REVISION 2

Constraints on deep, CO_2-rich degassing at arc volcanoes from solubility experiments on hydrous basaltic andesite of Pavlof Volcano, Alaska Peninsula, at 300 to 1200 MPa

Margaret T. Mangan[1*], Thomas W. Sisson[1**], W. Ben Hankins[1], Nobumichi Shimizu[2], Torsten Vennemann[3]

[1] U.S. Geological Survey, 345 Middlefield Road, Mail Stop 310, Menlo Park, California 94025 U.S.A.

[2] Woods Hole Oceanographic Institution, Mail Stop 23, 266 Woods Hole Road, Woods Hole, Massachusetts, 02543-1050 U.S.A

[3]University of Lausanne, Institute of Earth Surface Dynamics, CH-1015 Lausanne, Switzerland

[*] Retired

[**] Corresponding author (tsisson@usgs.gov)

Abstract

The solubility of CO_2 in hydrous basaltic andesite was examined in f_{O_2}-controlled experiments at a temperature of 1125 °C and pressures between 310-1200 MPa. Concentrations of dissolved H_2O and CO_2 in experimental glasses were determined by ion microprobe calibrated on a subset of run glasses analyzed by high temperature vacuum manometry. Assuming that the solubility of H_2O in mafic melt is relatively well known, estimates of $X_{H_2O}^{fluid}$ and $P_{H_2O}^{fluid}$ in the saturating fluid were modelled, and by

difference, values for $X_{CO_2}^{fluid}$ and $P_{CO_2}^{fluid}$ were obtained ($X_{CO_2} \sim 0.5 - 0.9$); f_{CO_2} could be then calculated from the fluid composition, temperature, and pressure.

Dissolved H_2O over a range of 2.3–5.5 wt.% had no unequivocal influence on the dissolution of CO_2 at the pressures and fluid compositions examined. For these H_2O concentrations, dissolved CO_2 increases with f_{CO_2} following an empirical power-law relation: dissolved $CO_2\ (ppmw) = 14.9^{+4.5}_{-3.5}\ [f_{CO_2}\ (MPa)]^{0.7\pm0.03}$. The highest pressure results plot farthest from this equation but are within its 1 standard-error uncertainty envelope.

We compare our experimental data with three recent CO_2-H_2O solubility models: Papale et al. (2006), Iacono-Marziano et al. (2012), and Ghiorso and Gualda (2015). The Papale et al. (2006) and Iacono-Marizano et al. (2012) models give similar results, both over-predicting the solubility of CO_2 in a melt of the Pavlof basaltic andesite composition across the f_{CO_2} range, whereas the Ghiorso and Gualda (2015) model under-predicts CO_2 solubility. All three solubility models would indicate a strong enhancement of CO_2 solubility with increasing dissolved H_2O not apparent in our results. We also examine our results in the context of previous high-pressure CO_2 solubility experiments on basaltic melts. Dissolved CO_2 correlates positively with mol fraction (Na+K+Ca)/Al across a compositional spectrum of trachybasalt—alkali basalt—tholeiite—icelandite—basaltic andesite. Shortcomings of current solubility models for a widespread arc magma type indicate that our understanding of degassing in the deep crust and uppermost mantle remains semi-quantitative. Experimental studies systematically varying concentrations of melt components (Mg, Ca, Na, K, Al, Si) may be necessary to identify solubility

reactions, quantify their equilibrium constants, and thereby build an accurate and generally applicable solubility model.

Keywords

experimental petrology, magmatic CO_2, volcanic degassing, volatile solubility

Introduction

Many studies address the systematics of magmatic degassing in shallow crustal reservoirs and volcanic conduits yet few are focused on degassing in the deep roots of volcanic systems. Understanding the behavior of C-O-H supercritical fluids in sub-arc magma at elevated pressures is important to a diverse suite of topics. Such knowledge is required to accurately assess volcanic volatile budgets and magma supply rates; model the linkage between basaltic underplating and remobilization of crystal mushes; interpret deep, long-period seismicity and tremor; and to characterize the thermodynamics of lower crustal melting.

Continued progress on these, and a host of other important research fronts, necessitate a more comprehensive and quantitative assessment of CO_2 solubility in hydrous mafic magmas at deep- to mid-crustal conditions. Due to the complexity of high temperature-high pressure experiments using mafic melts, relevant data are limited to a handful of studies − Jakobsson (1997), Liu et al. (2005), Botcharnikov et al. (2005), Behrens et al. (2009), Shishkina et al. (2010), Vetere et al. (2011), Iacono-Marziano et al. (2012), Iacovino et al. (2013), Allison et al. (2019) − and the thermodynamic and empirical models used to predict C-O-H solubilities in magma at pressures above ~500

MPa (e.g., Papale et al., 2006; Iacono-Marziano, 2012; Duan, 2014; Ghiorso and Gualda, 2015) have scant data to constrain them.

With the intent of building a stronger framework for understanding deep, CO_2-rich degassing of sub-arc magma, we conducted f_{O_2}-buffered solubility experiments at 1125 °C between 310 MPa to 1200 MPa total pressure using a hydrated basaltic andesite lava from Pavlof volcano, one of the most active centers in the Alaskan Aleutian Arc. We also conducted a small subset of decompression experiments to assess the ease of degassing and CO_2 re-equilibration during magma ascent.

Our oxygen-buffered, fluid-saturated experiments involved equilibration and degassing of fully molten natural basaltic andesite with C-O-H fluids in a piston-cylinder apparatus in the U.S. Geological Survey (USGS) Magma Dynamics Laboratory in Menlo Park, California. Volatile concentrations were measured in the quenched melts via ion microprobe calibrated with a subset of glasses with dissolved H_2O and CO_2 concentrations determined by high-temperature vacuum manometry. A few runs were also examined by Fourier-transform infrared spectroscopy (FTIR), but this method proved imprecise at the high dissolved CO_2 concentrations. Compositions of the excess fluid in equilibrium with the melt were estimated by application of relatively well-known H_2O solubility relations, as described subsequently.

Methods

Experimental techniques

The experiments use a natural basaltic andesite lava erupted from Pavlof volcano, one of six overlapping arc-front volcanoes within the Quaternary Emmons Lake Volcanic

Center on the lower Alaska Peninsula (Mangan et al., 2009). With at least 38 eruptions in the past 200 years, it is one of the most active volcanoes in the Aleutian arc. Pavlof lava is an advantageous composition to use in these experiments because quasi-steady magma supply rates, short magma-residence times, and limited interaction with host rocks preserve compositions of magmas ascending from deep-crustal storage.

Lava sample 03S75M1 of Mangan et al. (2009) was used in experiments. The flow from which the sample was extracted is mildly vesicular (7 vol.%) and hosts sub-millimeter phenocrysts composed of ~10 vol.% plagioclase ($An_{60\text{-}70s}$), 5 vol.% augite + hypersthene, and 1 vol.% olivine (Fo_{70s}). Antecrysts of anorthitic plagioclase of millimeter size are randomly scattered through the flow. The bulk composition of the starting material is listed in Table 1.

Table 1 near here

Rock powder previously prepared for XRF analysis was reground by hand in agate under triple-distilled water to a non-gritty talcum powder-like feel (generally less than 10 microns), then dried and stored in a laboratory oven at 110 °C. To improve precision of H_2O additions and to avoid loss of water during welding, this nominally anhydrous rock powder was mixed with ground, previously hydrated glass created from the same sample. Hydrous glass "spikes" were produced by loading and welding shut 5-mm-diameter Au capsules filled with 92 wt.% nominally dry rock powder and 8 wt.% triple-distilled water (200 mg total weight). The sealed capsules were held at 1050 °C at 1200 MPa in a piston-cylinder apparatus for 5–8 hours before rapid quenching to bubble-

115 free glass. The resulting hydrous glass spike was ground and added to the dried
116 nominally anhydrous rock powder to obtain the desired initial component of H_2O. The
117 CO_2 was added to the mixed dry+hydrous powders as Ag oxalate proportioned to deliver
118 a consistent 1 wt.% CO_2 to the starting mix.

119 The experiments were conducted using a modified double-capsule configuration
120 in which 40 mg of starting material comprising a mix of nominally dry rock powder and
121 the hydrous glass spike in proportions intended to deliver 2 wt.%, 4 wt.%, or 6 wt.% H_2O
122 depending on the run. The mixed starting powder and 1.5 mg Ag oxalate was packed
123 into a 3-mm-diameter $Ag_{70}Pd_{30}$ capsule snugly sheathed in thin-walled Pt tubing to
124 prevent physical contact of the inner capsule with the Ni-NiO buffer used to regulate
125 oxygen fugacity. The sheathed capsule was welded shut at one end using a graphite arc
126 welder. Once filled, the open end of the sheathed capsule was then crimped, the
127 previously sealed lower end placed in an ice bath, and the open end closed by arc
128 welding.

129 Each inner capsule was tested for leaks by weighing, heating, and re-weighing.
130 Sealed sample capsules were then placed in a 5-mm-diameter, Pt outer capsule packed
131 with 190 mg of a 1:1 (wt.) Ni-NiO buffer and 5 mg of a C-O-H source. The C-O-H
132 source was added to the outer capsule to fix the f_{H_2} in the inner capsule by diffusion, and
133 through this control the sample f_{O_2} by reproducing mol fractions of H_2O and CO_2 in the
134 buffer fluid to match the anticipated mol fractions of H_2O and CO_2 of the fluid inside the
135 sample capsule at equilibrium. The anticipated fluid composition in equilibrium with the
136 melt was estimated from the solubility model of Papale et al. (2006) for specific run

conditions. The C-O-H buffer added to the outer capsule was either a mix of Ag oxalate plus anhydrous oxalic acid, or was pure oxalic acid di-hydrate as shown in Table 2.

Table 2 near here

The expected yields of CO_2 released by decarbonation of Ag oxalate, anhydrous oxalic acid, and oxalic acid di-hydrate were confirmed by loading and welding those components into flattened Pt capsules. The sealed capsules were weighed and then heated with a propane-air flame until they expanded, indicating thermal decomposition of their contents. Upon cooling to room temperature, the capsules were reweighed, those that leaked were discarded, and sealed capsules were placed in a freezer overnight to condense and freeze H_2O. Upon removal from the freezer, the exterior of each capsule was wiped dry to remove condensation and punctured to release the evolved CO_2 gas. The capsule was then re-weighed to determine weight percent CO_2 lost and then placed in a 110 °C oven to vaporize and release the H_2O component of the decarbonation reaction. Finally, the capsule was removed from the oven and re-weighed. The mass balances showed the CO_2 liberated during decarbonation of Ag oxalate was within 4 % of the expected stochiometric yield; the CO_2/H_2O yield for oxalic acid di-hydrate was within 2 % of the expected stochiometric yield; and decarbonation of anhydrous oxalic acid liberated CO_2 gas within 7 % of the expected stochiometric yield.

We chose an above-liquidus run temperature of 1125 °C; lower temperature runs at 1050 °C and 1100 °C crystallized stable pyroxene and plagioclase or produced glasses with quench crystals. Isothermal experiments at 310–1200 MPa were conducted in a

one-inch, end-loaded, solid-media, piston-cylinder apparatus with a graphite furnace and pressed-CaF_2 assembly (e.g., Sisson et al., 2005; Blatter et al., 2013). The hydraulic line of the piston cylinder was linked to an argon gas reservoir permitting small, precise adjustments to pressure during equilibration and controlled pressure release during decompression runs (Lautze et al., 2010). While the runs were intended to be at even 100 MPa values, subsequent refinement of the pressure calibration using the CsCl melting technique (Bohlen, 1984) led to the recalculated final pressure values reported in our results.

In both solubility and decompression experiments, capsules were aligned perpendicular to the long axis of the furnace bore and positioned in the predetermined thermal maximum. The temperature gradient across the capsule was < 6 °C. Temperature was controlled using an S-type thermocouple (Pt-$Pt_{90}Rh_{10}$) positioned at the medial axis of the capsule. Run temperatures varied by < 1 °C during the experiments. Pressure was calibrated by bracketing the melting curve of thoroughly dried CsCl to within ± 2.5 MPa at 400, 800, and 1200 MPa after Bohlen (1984). Overnight variations in room temperature led to minor pressure changes (≤ 10 MPa) during runs that were adjusted such that runs were at their reported pressures for at least several hours before quenching.

Runs were equilibrated at temperature and pressure for 24 ± 1 hr. Solubility experiments were quenched immediately after equilibration. Decompression experiments underwent controlled pressure reduction (120–160 MPa/s) after equilibration at the initial pressure and then held a final pressure for a time of < 1 s to 3750 s depending on the run. In both types of experiments, rapid quenching was accomplished by abruptly turning off current to the furnace. The measured quench rate for the piston cylinder is a decrease of

40–70 °C/s (Bista et al., 2015). Each capsule was punctured and examined with a binocular microscope to assure that the Ni-NiO buffer was not exhausted during the run and that the fluid buffer was present.

We note here that additional carbon can be unintentionally introduced to runs in detectable amounts via diverse mechanisms such as non-stochiometric yields of Ag oxalate, capsule welding, the piston cylinder's graphite furnace assembly, trace organic contaminants in the rock powder, and possible metal-drawing compounds trapped during tubing manufacturing. For example, using the same experimental equipment, Blatter et al. (2013) report incorporation of 650 ± 70 ppm CO_2 in hydrous basalt during rapid fusion (10 min) experiments conducted at 900 MPa and 1,350 °C using $Au_{75}Pd_{25}$ capsules. In addition to the potential for absorption of atmospheric water; high temperature experiments are also subject to unintentional H_2O additions from reduction of ferric into ferrous iron (Holloway et al., 1992). Lense et al. (2011) report unintentional hydration of alkali basalt melts ranging non-systematically between 0.7–1.3 wt.% H_2O in CO_2-solubility experiments conducted at 1200 °C and 20–200 MPa (Pt capsules; 4–8 hr run duration; internally heated pressure vessel). In this study, blank experiments (Pavlof powder without added Ag oxalate or water) were run to evaluate such artifacts. Nominally dry rock powders (stored at 110 °C) were encapsulated in Pt and held at 1250 °C and 885 MPa for 10 minutes and then quenched to glass. We find that unintentional volatile additions may reach 0.8–1.1 wt.% H_2O and 1100–1120 ppm CO_2 in our experiments (see results section).

205 **Compositional Determinations**

206 Major-element compositions of run glasses were determined using the USGS
207 JEOL 8900 electron microprobe in Menlo Park, California operated at an accelerating
208 voltage of 15 kV. Alkali loss was minimized using a 2-nA beam current, a 10-µm spot,
209 and a 10-s counting time for Na. A variety of natural and synthetic minerals including
210 basaltic glass VG-A99 (Jarosewich et al., 1980) were used as standards, and background-
211 corrected count rates were converted to concentration with the JEOL proprietary version
212 of the CITZAF reduction routine (Armstrong, 1995). Glass analyses involved regularly
213 spaced traverses along and across the capsule length to test for glass homogeneity.

214 High-temperature, vacuum-extraction manometric measurements of dissolved
215 H_2O and CO_2 were made at the University of Lausanne, Institute of Mineralogy and
216 Geochemistry, Lausanne, Switzerland. Hydrogen and carbon concentrations (reported as
217 wt.% H_2O and CO_2) were analyzed in glasses from four basaltic andesite experiments
218 equilibrated at: 1015, 880, 815, and 520 MPa with 1 wt.% added CO_2 and 1 wt.% or 4
219 wt.% added H_2O. These melts coexisted with excess H_2O-CO_2 fluid but glass splits
220 selected for analysis were visibly bubble-free. The method used, modified from
221 Vennemann and O'Neil (1993), included transferring crushed, cleaned, and weighed
222 glass powders to silica tubes. Each sample was covered with previously outgassed quartz
223 grains and silica wool and then held at 10^{-6} mbar at 50 °C for at least 12 h to remove
224 surface H_2O. Samples were then heated to temperatures in excess of 1400 °C using an
225 oxygen-propane torch until no further gas was released. Released volatiles were
226 condensed in a liquid nitrogen trap (–196 °C). Non-condensable volatiles, including any
227 reduced H or C species, were oxidized by CuO (at 700 °C). H_2O and CO_2 were

subsequently separated using ethanol-liquid nitrogen slush traps (held at about –85 °C). The total CO_2 was then measured using a calibrated electronic manometer. The H_2O was transferred and sealed into a glass tube that contained Zn metal and was heated to 500 °C to produce H_2 for subsequent measurement using a Finnigan MAT 253 mass spectrometer. Weighed amounts of H_2O were always run in parallel with the samples to correct for daily variations in the tuning and sensitivity of the mass spectrometer. Although measurements were not replicated for individual samples, experience in the laboratory indicates uncertainties of about 2 % of measured concentrations for H_2O and 5 % of measured concentrations for CO_2.

Ion microprobe analyses were obtained for dissolved H_2O and CO_2 using the Cameca 1280 ion mass spectrometer (IMS) at the Northeast National Ion Probe Facility at Woods Hole Oceanographic Institution, Woods Hole, Massachusetts. Polished slices of the experimental glasses were mounted in an indium substrate to reduce carbon and hydrogen backgrounds. Analytical conditions include: Cs+ primary beam ~10 μm in diameter at 10 kV accelerating voltage and 1–2 nA of beam current, 30 x 30 raster size (μm), 4-minute pre-sputtering, and 20 cycle data. Measurements on our internal standards (glass splits from run products analyzed by manometry), combined with in-house subaerially degassed mafic glasses, provided working curves for calculation of H_2O and CO_2 concentrations in our unknowns.

Volatile concentration measurements were also attempted on a few glasses by Fourier-transform infrared spectroscopy at the USGS Volatile Laboratory in Menlo Park, California. The lab has a Nicolet Magna 750 FTIR with a SpectraTech Analytical-IR microscope attachment containing a liquid-nitrogen-cooled MCT-A detector. Spectra

This is the peer-reviewed, final accepted version for American Mineralogist, published by the Mineralogical Society of America.
The published version is subject to change. Cite as Authors (Year) Title. American Mineralogist, in press.
DOI: https://doi.org/10.2138/am-2021-7531. http://www.minsocam.org/

were acquired on 100-µm spots from 512 scans collected at 4-cm^{-1} resolution between 500 cm^{-1} and 4000 cm^{-1}. Dissolved water concentrations were calculated with Beer's Law (Dixon et al. 1995) using the H_2O_{total} peak (3530 cm^{-1}) with an extinction coefficient of 63 l/mol-cm (Dixon et al., 1995), but many samples could not be thinned sufficiently to avoid detector saturation. Carbon dioxide concentrations were calculated using the $CO_3^=$ doublet peaks (1515 and 1430 cm^{-1}) with an extinction coefficient of 375 l/mol-cm based on basalt glass (Fine and Stolper, 1986). As other researchers have noted, precise, but not necessarily accurate, baselines can be fitted to $CO_3^=$ doublets. We followed the curved-baseline methods described in King and Holloway (2002) to estimate maximum and minimum concentration for each doublet and report the average of the two as CO_2 in our data tables. A glass density of 2640 kg/m^3 was determined from glass composition and used in our calculations. Agreement can be poor between CO_2 concentrations measured by manometrically calibrated IMS and by FTIR, pointing to the aforementioned difficulties defining accurate FTIR backgrounds in the carbonate region.

Attempts were made to extract and measure the composition of the gas/fluid phase in equilibrium with the melt using inductively coupled plasma mass spectrometry (micro-ICPMS), but these efforts failed to produce reproducible results due to the small amount of excess vapor present at the end of our runs. Masses of quenched excess fluid were not measured, due to the difficulty of cleaning inner capsules of buffer and the likelihood of fluid trapped in vesicles along capsule walls, but rough values from mass-balance indicate low quantities, generally ≤ 1 mg and certainly < 2 mg. Calculations of fluid composition by mass-balance also proved of insufficient precision due to the aforementioned uncertainties in total H_2O and CO_2 concentrations; the mass-balance

This is the peer-reviewed, final accepted version for American Mineralogist, published by the Mineralogical Society of America.
The published version is subject to change. Cite as Authors (Year) Title. American Mineralogist, in press.
DOI: https://doi.org/10.2138/am-2021-7531. http://www.minsocam.org/

approach propagates analytical, weighing, and other uncertainties onto the fluid's apparent composition, and these are magnified by the fluid's low mass fraction. In lieu of direct measurement, the mol fraction of CO_2 in the co-existing fluid phase was estimated building on the approach of Iacono-Marziano et al. (2012) in which the fluid is treated as a binary mixture of H_2O and CO_2 for which total pressure (LHS in Eqn. 1) is the sum of the partial pressures of the mixed fluid (RHS in Eqn. 1) with the partial pressure of CO_2 in the mixed fluid converted to mol fraction as in Eqn. 2:

$$P_{total} = P_{H_2O}^{mixed\ fluid} + P_{CO_2}^{mixed\ fluid} \quad \text{Eqn. 1}$$

$$X_{CO_2}^{mixed\ fluid} = P_{CO_2}/P_{total} \quad \text{Eqn. 2}$$

The CO_2 fugacity (f_{CO_2}) can then be calculated from the fluid bulk composition, temperature, and total pressure using an appropriate mixed-fluid equation of state.

The partial pressure of H_2O in the mixed fluid ($P_{H_2O}^{mixed\ fluid}$) is approximated by applying a solubility model to derive the mol fraction of H_2O in a mixed H_2O-CO_2 fluid that would yield the dissolved H_2O concentration measured in our experimental melts at each synthesis temperature and total pressure. This approach assumes that (1) the effects of melt composition, pressure, and temperature on H_2O solubility are adequately known, and (2) dissolved CO_2 is of insufficient abundance in the melt to influence dissolved H_2O at high pressure as per Ni and Keppler (2013). The solubility models of Ghiorso and Gualda (2015) and of Papale et al. (2006) were applied to derive two estimates of $X_{H_2O}^{mixed\ fluid}$ and $X_{CO_2}^{mixed\ fluid}$, and from these, $P_{H_2O}^{mixed\ fluid}$ and $P_{CO_2}^{mixed\ fluid}$, then f_{CO_2}, in

This is the peer-reviewed, final accepted version for American Mineralogist, published by the Mineralogical Society of America.
The published version is subject to change. Cite as Authors (Year) Title. American Mineralogist, in press.
DOI: https://doi.org/10.2138/am-2021-7531. http://www.minsocam.org/

297 both cases with ferric and ferrous iron in the melt set for an f_{O_2} of Ni-NiO at 1125 °C
298 (Kress and Carmichael, 1988).

299 The practical approach was to enter the Pavlof melt composition into the
300 software-application version of those solubility models, then adjust the H_2O and CO_2
301 concentration values so that the melt would be saturated at each run's synthesis
302 temperature and total pressure with a trace (≤ 0.1 wt.%) of H_2O-CO_2 fluid, with the
303 melt's predicted dissolved H_2O concentration matching that measured in each glass. The
304 dissolved CO_2 concentrations predicted by the models at those conditions were not
305 required to match measured values, since CO_2 solubility was the aspect potentially
306 requiring revision. Both solubility models employ non-ideal equations of state for the
307 fluid to derive H_2O and CO_2 fugacities, but the software applications of those models
308 report the saturating fluid's estimated composition ($X_{CO_2}^{mixed\ fluid}$, $X_{H_2O}^{mixed\ fluid}$) not those
309 underlying fugacities. The fluid compositions reported by the two saturation models
310 were therefore used to calculate two estimates of CO_2 fugacity for each run at its
311 synthesis conditions using the non-ideal mixed fluid fugacity model of Churakov and
312 Gottschalk (2003a, b) (at http://fluid-eos.web.psi.ch/EOS/calculator_simple.html). Spot
313 comparisons show close agreement of the obtained f_{CO_2} with values derived with the
314 CORK H_2O-CO_2 fluid model of Holland and Powell (1991, 2003), and the Allison et al.
315 (2019) MATLAB calculator that employs a modified Redlich-Kwong equation of state
316 corrected for high pressure after Saxena and Fei (1987). The Papale et al. (2006)
317 solubility model is calibrated to 1000 MPa, so for higher run pressures the partial
318 pressure of H_2O necessary at 1000 MPa to yield the measured dissolved H_2O
319 concentration was applied as the H_2O partial pressure at the higher total run pressure.

This is the peer-reviewed, final accepted version for American Mineralogist, published by the Mineralogical Society of America.
The published version is subject to change. Cite as Authors (Year) Title. American Mineralogist, in press.
DOI: https://doi.org/10.2138/am-2021-7531. http://www.minsocam.org/

Both solubility models treat the saturating fluid as a non-ideal binary mix of H_2O and CO_2, so effects of $X_{CO_2}^{mixed\ fluid}$ on f_{H_2O} are addressed internal to those models. A simpler approach for estimating f_{CO_2}, more similar to that of Lesne et al. (2011), was initially employed involving determining the total pressure at which each run would attain its measured dissolved H_2O concentration if saturated with pure H_2O, with that pressure then used as the H_2O partial pressure at run conditions, with $P_{CO_2}^{mixed\ fluid}$ and $X_{CO_2}^{mixed\ fluid}$ determined as in Eqns. 1 and 2. That approach does not, however, capture the increasingly non-ideal behavior of the mixed fluid with increasing pressure, leading to underestimates of f_{CO_2} to about 20 % relative that increase systematically with pressure, and so was abandoned. Differences in f_{CO_2} derived applying the Ghiorso and Gualda (2015) versus the Papale et al. (2006) models for H_2O solubility range from 4–20 % of their mean (average of 10.1 %, median of 8.9 %). Applying the Papale et al. (2006) model consistently yields greater f_{CO_2} values, with the difference generally increasing with dissolved H_2O concentrations, reflecting a lower $P_{H_2O}^{fluid}$ required by that model to achieve a specific dissolved H_2O concentration.

Results

General characteristics of the glasses

The major-element compositions of the quenched glasses are within the analytical uncertainty of the whole-rock XRF analysis of the starting material (c.f. Table 1 and Table 3) except FeO_{total}, which is ~0.5 wt.% lower in run products. All glasses are translucent brown and crystal-free. Solubility runs produced bubble-free glass, with a

few minute scallops at the capsule wall where excess gas/fluid pooled during the run. Rapid decompression followed by immediate quench produced glass with sparse, difficult-to-discern bubble embryos (#1916), and at increasing dwell times at P_{final}, vesiculated glass with textures suggesting an initially uniform distribution of bubbles (run #1919) that then segregated toward the top of the capsule (#1958, #1962). Number densities measured in bubble segregations (foam) decline with increasing hold times due to coalescence and ripening (see Lautze et al., 2010). Textures produced during decompression runs are described in Table 4 and illustrated in Figure 1.

Figure 1 and Tables 3-4 near here

Volatile components and concentrations

Glasses from several experiments were analyzed via FTIR to determine the molecular form of the volatiles dissolved in the glass. For some samples, well-defined peaks were observed for H_2O_{total} (3500 cm^{-1}), $H_2O_{molecular}$ (5200 cm^{-1}), and OH^- (4519 cm^{-1}). Relative peak heights suggest ≥ 62 % of the water dissolved in the melt was in the form of OH^- at the point speciation was locked during quenching. Dissolved carbon in quenched glass manifests as $CO_3^{=}$ doublets (1500 cm^{-1} and 1422 cm^{-1}), with symmetries and peak-to-peak distances constant across a range of experimental pressures and volatiles. A minor CO_2 absorbance peak (2350 cm^{-1}) occurs in several spectra, but in all cases would constitute ≤ 1.3 % of the total dissolved carbon, and contamination of the measurements by atmospheric CO_2 cannot be excluded. An example of a well-resolved spectrum is given in Figure 2.

365

366 *Figure 2 near here*

367

368 Concentrations of dissolved H_2O and CO_2 were estimated from FTIR spectra for a
369 handful of experimental glasses, but our primary dataset, provided in Table 5, comes
370 from ion microprobe measurements calibrated on Pavlof reference glasses measured by
371 manometry.

372 In some run glasses excess dissolved H_2O and/or CO_2 is indicated; that is, the
373 dissolved volatile concentration measured in the glass by ion probe exceeds that
374 originally added to the capsule. Although unintentional presence of H_2O and CO_2 is
375 indicated by our blank experiments (runs #1903A and #1913A in Table 5), we cannot
376 rule out another possibility that C and H from the fluid buffer infiltrated the inner
377 capsule. The ease of C and H diffusion through Pt capsules (and Pd) is well known (e.g.,
378 Brooker et al., 1998); high-pressure infiltration through Ag-Pd alloys is expected to be
379 slower, but exact rates are unknown.

380

381 *Table 5 near here*

382

383 Data from Table 5 are plotted in Figs. 3, 4, 5, and 6. Measured concentrations of
384 dissolved H_2O and CO_2 for each pressure (Fig. 3) resemble saturation isobars familiar
385 from other solubility studies, with nearly constant to weakly declining CO_2
386 concentrations with increasing dissolved H_2O over the range of H_2O concentrations
387 investigated. Ni and Keppler (2013) reviewed results from the limited number of C-O-H

388 solubility experiments published for mafic melts at high pressure and made a similar
389 observation, noting that at pressures ≥500 MPa "CO_2 solubility is nearly constant [within
390 uncertainties] over a broad H_2O concentration range [~1-5 wt.% H_2O]." Figure 4 shows
391 dissolved CO_2 concentrations plotted versus total pressure, dissolved H_2O concentrations
392 plotted versus estimated $P_{H_2O}^{fluid}$, and dissolved CO_2 concentrations plotted versus
393 estimated $P_{CO_2}^{fluid}$. Values for $P_{H_2O}^{fluid}$ and $P_{CO_2}^{fluid}$ are simply $P_{total} \times X_{H_2O}^{mixed\ fluid}$ and
394 $P_{total} \times X_{CO_2}^{mixed\ fluid}$ and are plotted as the mid-points and ranges of the fluid
395 compositions derived with the Papale et al. (2006) and Ghiorso and Gualda (2015)
396 solubility models. Dissolved H_2O concentrations increase at close to the canonical
397 square root of P_{H_2O} relation long known from experimental studies for fluid-saturated
398 melts at low pressure or with $X_{H_2O}^{fluid} < 0.5$ (Hamilton et al., 1964; Burnham 1979). Both
399 the Ghiorso and Gualda (2015) and Papale et al. (2006) solubility models require slightly
400 greater $P_{H_2O}^{fluid}$ at greater total pressure to attain the same dissolved H_2O concentration
401 (Fig. 4B). Since $P_{CO_2}^{fluid}$ is estimated by difference and our higher H_2O melts were
402 produced at greater total pressures (Table 5), this also appears as slightly lower
403 $P_{CO_2}^{fluid}$ values to attain the same dissolved CO_2 concentrations in higher-H_2O melts (Fig.
404 4C).

405 Solubilities are more appropriately referenced to fugacities, with CO_2 fluid being
406 strongly non-ideal at high pressures where $f_{CO_2} \gg P_{CO_2}^{fluid}$. Fugacities can be expressed as
407 in Eqn. 3:
408

409 $$f_{CO_2} = \gamma_{CO_2} \times P_{CO_2}^{mixed\ fluid} \qquad \text{Eqn. 3}$$

This is the peer-reviewed, final accepted version for American Mineralogist, published by the Mineralogical Society of America.
The published version is subject to change. Cite as Authors (Year) Title. American Mineralogist, in press.
DOI: https://doi.org/10.2138/am-2021-7531. http://www.minsocam.org/

Where γ_{CO_2} is the fugacity coefficient for CO_2, and similarly for H_2O, although in the present case fugacities were obtained directly from fluid composition and intensive conditions using the software application version of the of Churakov and Gottschalk (2003a, b) mixed fluid equation of state (at http://fluid-eos.web.psi.ch/EOS/calculator_simple.html) without need of the intermediate step of deriving γ_{CO_2}. Figure 5 illustrates the relation between f_{CO_2} and total pressure, that the drier melts coexisted with drier fluids, and that all the fluids were relatively H_2O-poor. Figure 6 shows that dissolved CO_2 concentrations increase with increasing f_{CO_2} (Ghiorso and Gualda-based derivation) following a power-law relation that is robust to about f_{CO_2} = 14000 MPa (total pressure greater than ~1000 MPa). Higher-pressure results plot farther from the regression line but remain within its propagated uncertainty envelope, and no strong association is apparent between dissolved H_2O concentrations and CO_2 solubility.

Figures 3-4-5-6 near here

Implications

Comparing experiments and solubility models

In Figure 7 we compare our experimental data with results from three recent and conveniently available CO_2-H_2O solubility models: Papale et al. (2006), Iacono-Marziano et al. (2012), and Ghiorso and Gualda (2015). The thermodynamic model of Papale et al. (2006) evaluates the excess Gibbs free energy of coexisting melt + vapor with the melt

phase treated as a non-isometric mixture of 8 major-element oxides, H_2O, and CO_2. The Iacono-Marziano et al. (2012) model is a semi-empirical formulation for the solubility of C-O-H fluids based on structural properties, with dissolved CO_2 concentrations determined by the number of non-bridging oxygen per oxygen (NBO/O) and the type of charge balancing cations present in the melt, with the relative positive influence of Na^+, $K^+ > Ca^{++} >> Mg^{++}$ on dissolved CO_2. Ghiorso and Gualda (2015) incorporate H_2O and CO_2 solubility into the regular-solution model formalism of the MELTS thermodynamic software assemblage with the simplifications that dissolved H_2O is fully dissociated into hydroxyl units and that CO_2 dissolves as both molecular CO_2 and carbonate units, the latter associated solely with Ca as a $CaCO_3$ component. Ghiorso and Gualda (2015) recognize that dissolved carbonate is also associated with other elements (Na, K, Mg) but note that insufficient experiments have been performed to model their activities.

Results for the Papale et al. (2006), Iacono-Marziano et al. (2012), and Ghiorso and Gualda (2015) solubility models are shown in Figure 7 for a melt of Pavlof basaltic andesite composition with 2, 4, and 6 wt.% dissolved H_2O. The Papale et al. (2006) and Iacono-Marziano (2012) results are similar to each other, and both overestimate the solubility of CO_2 in Pavlof basaltic andesite melt across the entire investigated range of f_{CO_2}, whereas the Ghiorso and Gualda (2015) model matches the measured trend of CO_2 concentrations with f_{CO_2} up to about 5000 MPa but underestimates CO_2 concentrations at greater f_{CO_2} values. Disparities between the individual models, and with the Pavlof measurements, are likely due to the limited numbers of experimental solubility determinations upon which the models rest (Moore, 2008; Ghiorso and Gualda, 2015), particularly for higher pressures, and to the lack of studies that systematically vary

456 concentrations of melt components that are likely to control CO_2 solubility, precluding
457 adequately separating and characterizing their influences.
458
459 *Figure 7 near here*
460
461 In detail, each solubility model can be displayed as a power-law relation between
462 dissolved CO_2 and f_{CO_2}, and each such curve shifts to higher dissolved CO_2
463 concentrations at higher dissolved H_2O concentrations (Fig. 7). Shifts to higher dissolved
464 CO_2 with higher dissolved H_2O (for a given f_{CO_2}) are larger in the models than is obvious
465 from the Pavlof measurements, although such a shift is suggested by the highest f_{CO_2}
466 Pavlof results. The cause of the model shift is two-fold. Recent syntheses of CO_2-H_2O
467 solubility in silicate melts (Papale et al., 2006; Iacono-Marziano et al., 2012; Ni and
468 Keppler, 2013; Duan, 2014; Ghiorso and Gualda, 2015) derive an enhancement of fluid-
469 saturated melt CO_2 concentrations at low to intermediate melt H_2O concentrations, seen
470 as an arching or doming of CO_2-H_2O concentration isobars (Fig. 8). Isobar doming
471 becomes conspicuous at fluid-saturation pressures greater than about 500 MPa, with peak
472 CO_2 concentrations also shifting to higher H_2O concentrations at greater fluid-saturation
473 pressures. The second, subtle, but more general factor is that isopleths of constant f_{CO_2}
474 have positive slopes across most of the relevant fluid-saturated CO_2-H_2O concentration
475 space (CO_2: ordinate, H_2O: abscissa), such that they intersect higher-pressure saturation
476 isobars at greater concentrations of both dissolved H_2O and CO_2 (Fig. 8). For a given
477 f_{CO_2}, higher H_2O concentrations in the melt, therefore, require higher CO_2 concentrations
478 and higher saturation pressures, irrespective of the presence or magnitude of H_2O-

induced doming of saturation isobars. Enhancement of CO_2 solubility by addition of H_2O (isobar doming) is not obvious in the experimental H_2O and CO_2 concentrations of fluid saturated Pavlof basaltic andesite melt (Fig. 3), but a slight enhancement is suggested by relations between CO_2 concentration and $P_{CO_2}^{fluid}$ (Fig. 4C), and is allowed but not required by relations between CO_2 concentration and f_{CO_2} (Fig. 6). No experiments were conducted of the solubility of pure CO_2 fluid that would more clearly reveal a presence and magnitude of H_2O's ability to enhance CO_2 solubility, but our results do indicate that enhancements are less at high pressure than would be predicted by published H_2O-CO_2 solubility models (Fig. 7).

Figure 8 near here

Presently, it appears that the most judicious approach to simulating degassing of mafic magmas ascending from the uppermost mantle into the lower- and mid-crust may be to employ a range of solubility models and accept the uncertainty that comes from their differences, instead of employing a single model that may allow precise calculations that, nevertheless, can be appreciably inaccurate.

Influence of melt composition on CO_2 dissolution

Although several experimental studies using mafic compositions demonstrate positive correlation between the CO_2 solubility and melt alkalinity, recent experiments by Allison et al. (2019) caution that the correlation is not a "simple scaling." Using the approach of Iacono-Marziano et al. (2012), we employ their "agpaitic index" (mol

fraction (Na+K+Ca)/Al*; n.b.* agpaitic index is conventionally defined as molar (Na+K)/Al after Ussing (1912)) to examine a subset of our results in the context of previous high-pressure CO_2 solubility experiments for basaltic melts conducted under generally similar pressure-temperature-compositional conditions (Figs. 9 and 10).

Figures 9-10 near here

The "agpaitic indices" labelled in Fig. 9 correlate positively with CO_2 solubility. For a given f_{CO_2}, dissolved CO_2 is composition-dependent across a compositional spectrum of trachybasalt—alkali basalt—tholeiite—basaltic andesite. The correlation appears to hold at higher pressures as well, although the only experiments available for relevant comparison are a subset of Jakobsson (1997) for hydrous icelandite ("agpaitic index" 1.17) equilibrated at 1000 MPa total pressure and 1400 °C with 4.0–4.8 wt.% dissolved H_2O (Fig. 10).

For basaltic melts, CO_2 solubility is largely insensitive to temperature (Ni and Keppler, 2013), so differing synthesis temperatures should have little impact on the systematics displayed in Figs. 9 and 10. The implication is that a relatively small shift in melt composition can lead to significant difference in CO_2 solubility. At a fixed f_{CO_2} of 1000 MPa, for example, increasing the "agpaitic index" from 0.96 to 1.42 (Pavlof basaltic andesite to Etna trachybasalt) serves to increase the concentration of dissolved CO_2 by 190 %. The primitive Aleutian basalt ID16 from Adak Island (Nye and Reid, 1986) has "agpaitic index" of 0.88, similar to Pavlof basaltic andesite, so changes in CO_2 solubility may be small as parental arc basalts fractionate to basaltic andesites, but

additional solubility studies systematically covering the spectrum of natural mafic melts are needed before deep CO_2-rich degassing can be modeled confidently.

Decompression, vesiculation, and re-equilibration

Although few, our near-instantaneous decompression experiments provide insight into melt re-equilibration following vesiculation at high degrees of CO_2 supersaturation. The glass produced in run #1919 records homogeneous nucleation of 10^4 bubbles/mm^3 for a dwell time of 30 s at P_{final} for a CO_2 supersaturation ratio of ~6 (measured concentration of CO_2 at P_{final} / equilibrium concentration at P_{final}). Runs #1958 and #1962 show the supersaturation ratio at quench decreases with increasing time at P_{final} from ~3 (150 s at P_{final}) to ~1 (3750 s at P_{final}), suggesting that the time required to re-establish equilibrium is somewhere between a few hundred to a few thousand seconds in our experiments.

The quasi-uniform distribution of bubbles in run #1919 make it possible to estimate an effective diffusivity for CO_2 in hydrous basaltic andesite of 4.5×10^{-11} m^2/s. Our determination uses the expression given in Epel'baum et al. (1973)

$$D_{CO_2} = \left[\lambda^3 \rho_m \left(\omega_o - \omega_f\right)/\rho_{CO_2}\right]^{2/3} \tau^{-1} \qquad \text{Eqn. 4}$$

in which λ is the mean distance between bubbles (~[number density]$^{-1/3}$ = 4×10^{-5} m), ρ_m is melt density (2600 kg/m^3 at 310 MPa, 1125 °C, and 1.37 wt.% H_2O), ω_o, is the original weight fraction of dissolved CO_2 (0.0137 from run #2088), ω_f is final weight fraction of dissolved CO_2 at quench (0.0049 from Table 5), ρ_{CO_2} is the fractional density of CO_2

548 dissolved in the melt (~10 kg/m^3 assuming partial molar volume of CO_2 of $3.3x10^{-5}$
549 m^3/mol) and τ is the diffusion duration, timed from the start of decompression to quench
550 (62 s). Our empirical determination is consistent with that obtained using the argon
551 proxy formulation in Zhang and Ni (2010) for total effective binary diffusivity of CO_2,
552 which gives $1x10^{-11}$ m^2/s using pressure-temperature-compositional conditions consistent
553 with our experiments.

554 The peak bubble number density given in Table 4 is similar in magnitude to those
555 reported for natural samples of scoria ejected during dry (and wet) basaltic Plinian
556 eruptions (see summary in Mangan et al., 2014; Mastin, 1997; Mastin et al., 2004;
557 Polacci et al., 2006; Sable et al., 2006; Costantini et al., 2009 and 2010). While it is
558 tempting to equate the high bubble number density in our experiments to explosive,
559 disequilibrium degassing of CO_2 as a trigger for Plinian basaltic eruptions, saturation
560 depths of > 15 km and rapid re-equilibration make this an unlikely scenario. For basaltic
561 melts, Bottinga and Javoy (1991) show that a high supersaturation ratio (≥ 3) is required
562 for bubble nucleation in the shallow crust because the surface area of incipient bubbles is
563 relatively large at low pressure, whereas for the higher pressure conditions of the lower-
564 to mid-crust, the surface areas of incipient bubbles are smaller and the supersaturation
565 ratio needed for nucleation is low; bubbles nucleate readily in the lower- to mid-crust and
566 rapid re-equilibration follows suit (see review in Mangan et al., 2014). Several petrologic
567 studies suggest that magmas in the deep-crustal roots of many volcanic systems are
568 saturated with a free, CO_2-rich fluid phase (see review in Lowenstern, 2001), and our
569 experiments support this assertion. Released and accumulated in sufficient abundance,
570 these low-viscosity supercritical fluids could facilitate lower crustal magma transport by

571 opening tensile fractures in hot, pressurized country rock that might otherwise deform in
572 a ductile manner.
573
574 **Deep degassing of CO_2 in sub-arc magma**
575 Dissolved CO_2 concentrations in primary, un-degassed sub-arc basaltic melts
576 inferred from the ratio of carbon dioxide to noble gas (e.g., $CO_2/^3H$) in lavas,
577 hydrothermal fluids, and/or volcanic gas emissions span the range from 0.4 wt.% – 1.3
578 wt.% (Wallace, 2004; Fischer and Marty, 2004). Our solubility experiments demonstrate
579 that dissolved CO_2 concentrations as high as 1.3 wt.% are certainly feasible in mafic arc
580 magmas residing at depths near the continental Moho.
581 For Pavlof volcano, petrologic models indicate that basaltic andesite melts form in
582 a lower- to mid-crustal intrusive complex from high-alumina basaltic parents
583 fractionating clinopyroxene, spinel, and plagioclase at depths equivalent to 500 to 1000
584 MPa (Mangan et al., 2009). Seismic tomography supports this petrologic interpretation:
585 inversion of P-wave velocities from regional earthquakes reveals a crustal thickness of
586 about 40 km and the top of a low-velocity zone, inferred to be a region of 10–15 % melt,
587 at ~20 km (McNutt and Jacob, 1986). Infrequent long-period earthquakes are detected at
588 focal depths of between 20–40 km, presumed to be triggered by quasi-steady fluxing of
589 basaltic magmas, and by release and escape of their exsolved CO_2-rich fluids, in a deep
590 intrusive complex (Power et al., 2004). Using published magma-supply estimates for
591 Pavlof of 10^6–10^7 m^3/year characterizing the last several decades (McNutt and Beavan,
592 1987; Waythomas et al., 2017), liberation of 10^7–10^8 kg of magmatic CO_2 per year is
593 possible within a crustal volume of ~$3.5x10^8$ m^3, assuming originally CO_2-saturated

basalt or basaltic-andesite melt at 40 km, 2680 kg/m^3 melt density, and that the magmas degas large fractions of their CO_2 either by ascent and decompression or by large extents of solidification.

Basaltic melt inclusions (MIs) are rare in Pavlof's eruption scoria and the few analyzed samples offer little additional insight into the original concentration of CO_2 in its source magma. Mafic MIs contain ≤ 2.5 wt.% and ≤ 550 ppm dissolved H_2O and CO_2, respectively (Anderson, 1982; M. Zimmer, personal communication, 2006; Zimmer et al., 2010), but were trapped at low pressures in olivine and magnetite crystallizing at < 200 MPa in sub-volcanic feeders (Mangan et al., 2009).

The Pavlof experimental results allow for CO_2 concentrations in its basaltic andesite liquids in the range of ~1.4–0.1 wt.% for magmas residing at ~45 km to 15 km depth, respectively. A broad survey of melt-inclusion CO_2 concentrations published for hydrous, subduction-related basaltic compositions are mostly in the range 500–1500 ppm (see Fig. 9 in Métrich and Wallace, 2008), which when considered in tandem with the experiments herein, suggest that substantial CO_2-rich degassing occurs prior to MI entrapment in most arc magmas.

Acknowledgements

The design and interpretation of our experiments benefited from numerous discussions with Jake Lowenstern, Dawnika Blatter, Bill Evans, and Jennifer Lewicki. We appreciate Mindy Zimmer for sharing her unpublished melt inclusion data. We thank Gary Landis for his effort to extract compositions on gas/fluids using with micro-ICPMS. Peer-reviews by Jake Lowenstern, Kurt Roggensack, and Antonio Paonita, and Antonio

Acosta-Vigil's editorial comments and handling are greatly appreciated. This study was funded by the U.S. Geological Survey, Volcano Hazards Program with additional support from the Woods Hole Oceanographic Institution, Department of Geology and Geophysics, and the University of Lausanne, Institute of Mineralogy and Geochemistry. Any use of trade, firm, or product names is for descriptive purposes only and does not imply endorsement by the U.S. Government.

REFERENCES CITED

Allison, C.M., Roggensack, K., and Clarke, A.B. (2019) H_2O-CO_2 solubility in alkali-rich mafic magmas; new experiments at mid-crustal pressures. Contributions to Mineralogy and Petrology, 174:58. https://doi.org/10.1007/s00410-019-1592-4

Anderson, A.T. (1982) Parental basalts in subduction zones: implications for continental evolution. Journal of Geophysical Research, 87, 7047–7060.

Armstrong, J.T. (1995) CITZAF: a package of correction programs for the quantitative electron microbeam X-ray analysis of thick polished materials, thin films, and particles. Microbeam Analysis, 4, 177–200.

Behrens, H., Misiti, V., Freda, C., Vetere, F., Botcharnikov, R.E., and Scarloto, O. (2009) Solubility of H_2O and CO_2 in ultrapotassic melts at 1200 and 1250 °C and pressure from 50-500 MPa. American Mineralogist, 94, 105–120. doi:10.2138/am.2009.2796

Bista, S., Stebbins, J.F., Hankins, W.B., and Sisson, T.W. (2015) Aluminosilicate melts and glasses at 1 to 3 GPa: Temperature and pressure effects on recovered structural and density changes. American Mineralogist, 100, 2298–2307, doi.org/10.2138/am-2015-5258

640 Blatter, D.L., Sisson, T.W., and Hankins, W.B. (2013) Crystallization of oxidized,
641 moderately hydrous arc basalt at mid-to-lower-crustal pressures: implications for
642 andesite genesis. Contributions to Mineralogy and Petrology, 166, 861–886.
643 Bohlen, S.R. (1984) Equilibria for precise calibration and a frictionless furnace assembly
644 for the piston-cylinder apparatus. Neues Jahrbuch für Mineralogie. Monatshefte, 4,
645 404–412.
646 Botcharnikov, R., Freise, M., Holtz, F., and Behrens, H. (2005) Solubility of C-O-H
647 mixtures in natural melts: new experimental data and application to a range of
648 models. Annals of Geophysics, 48, 633–645.
649 Bottinga, Y., and Javoy, M. (1991) The degassing of Hawaiian tholeiite. Bulletin of
650 Volcanology, 53, 73–85.
651 Brooker, R., Holloway, J.R., and Hervig, R. (1998) Reduction in piston-cylinder
652 experiments: The detection of carbon infiltration into platinum capsules. American
653 Mineralogist, 83, 985–994.
654 Burnham, C.W. (1979) The importance of volatile constituents. In: H.S. Yoder, Ed., The
655 Evolution of Igneous Rocks, Fiftieth Anniversary Perspectives, p. 1077-1084,
656 Princeton University Press, Princeton, NJ.
657 Churakov, S.V., and Gottschalk, M. (2003a) Perturbation theory based equation of state
658 for polar molecular fluids: I. Pure fluids. Geochimica et Cosmochimica Acta, 67,
659 2397–2414.
660 Churakov, S.V., and Gottschalk, M., (2003b) Perturbation theory based equation of state
661 for polar molecular fluids: II. Fluid mixtures. Geochimica et Cosmochimica Acta, 67,
662 2415–2425.

663 Costantini, L., Bonadonna, C., Houghton, B.F., and Wehrmann, H. (2009) New physical
664 characterization of the Fontana Lapilli basaltic Plinian eruption Nicaragua. Bulletin of
665 Volcanology, 71- 3, 337–355, doi:10.1007/s00445-008-0227-9
666 Costantini, L., Houghton, B.F., and Bonadonna, C. (2010) Constraints on eruption
667 dynamics of basaltic explosive activity derived from chemical and microtextural
668 study: the example of the Fontana Lapilli Plinian eruption, Nicaragua. Journal of
669 Volcanology and Geothermal Research, 189, 207–224,
670 doi:10.1016/jvolgeores.2009.11.008
671 Dixon, J.E., Stolper, E.M., and Holloway, J.R. (1995) An experimental study of water
672 and carbon dioxide solubilities in Mid-Ocean Ridge basaltic liquids. Part I:
673 Calibration and solubility models. Journal of Petrology, 36, 1607–1631.
674 Duan, X. (2014) A general model for predicating the solubility behavior of H_2O-CO_2
675 fluids in silicate melts over a wide range of pressure, temperature, and compositions.
676 Geochimica et Cosmochimica Acta, 125, 582–609.
677 Epel'baum, M.B., Bababashov, I.V., and Salova, T.P. (1973) Surface tension of felsic
678 magmatic melts at high temperature and pressures, Geokhimiya, 3, 461–464.
679 Fine, G., and Stolper, E. (1986) Dissolved carbon dioxide in basaltic glasses:
680 concentrations and speciation. Earth and Planetary Sciences Letters, 76, 263–278.
681 Fischer, T.B., and Marty, B. (2004) Volatile abundances in sub-arc mantle: insights from
682 volcanic and hydrothermal gas discharges. Journal of Volcanology and Geothermal
683 Research, 140, 205–216.

684 Ghiorso, M.S., and Gualda, G.A.R. (2015) An H_2O-CO_2 mixed fluid saturation model
685 compatible with rhyolite-MELTS. Contributions to Mineralogy and Petrology,
686 169:53. https://doi.org/10.1007/s00410-015-1141-8
687 Hamilton, D.L., Burnham, C.W., and Osborn, E.F. (1964) The solubility of water and
688 effects on oxygen fugacity and water content on crystallization in mafic magmas.
689 Journal of Petrology, 5, 21–39.
690 Holland, T., and Powell, R. (1991) A Compensated-Redlich-Kwong (CORK) equation
691 for volumes and fugacities of CO_2 and H_2O in the range 1 bar to 50 kbar and 100-
692 1600C. Contributions to Mineralogy and Petrology, 109, 265–273.
693 Holland, T., and Powell, R. (2003) Activity-composition relations for phases of
694 petrological calculations: an asymmetric multicomponent formulation. Contributions
695 to Mineralogy and Petrology, 145, 492–501.
696 Holloway, J.R., Dixon, J.E., and Pawley, A.R. (1992) An internally heated, rapid-quench,
697 high-pressure vessel. American Mineralogist, 77, 643–646.
698 Iacono-Marziano, G., Morizet, Y., Le Trong, E., and Gaillard, F. (2012) New
699 experimental data and semi-empirical parameterization of H_2O-CO_2 solubility in
700 mafic melts. Geochimica et Cosmochimica Acta, 97, 1–23.
701 doi:10.1016/j.gca.2012.08.035
702 Iacovino, K., Moore, G., Roggensack, K., Oppenheimer, C., and Kyle, P. (2013) H_2O-
703 CO_2 solubility in mafic alkaline magma: applications to volatile sources and
704 degassing behavior at Erebus volcano, Antarctica. Contributions to Mineralogy and
705 Petrology, 166, 845–860. doi10.1007/s00410-013-0877-2

706 Jakobsson, S. (1997) Solubility of water and carbon dioxide in an icelandite at 1400 °C
707 and 10 kilobars. Contributions to Mineralogy and Petrology, 127, 129–135.
708 Jarosewich, E., Nelen, J.A., and Norberg, J.A. (1980) Reference standards for electron
709 microprobe analysis. Geostandards Newsletter, 4, 43–47.
710 King, P.L., and Holloway, J.R. (2002) CO_2 solubility and speciation in intermediate
711 (andesitic) melts: the role of H_2O and composition. Geochimica et Cosmochimica
712 Acta, 66, 1627–1640.
713 Kress, V.C., and Carmichael I.S.E. (1988) Stoichiometry of the iron oxidation reaction in
714 silicate melts. American Mineralogist, 73, 1267–1274.
715 Lautze, N.C., Sisson, T.W., Mangan, M.T., and Grove, T.L. (2010) Segregating gas from
716 melt: an experimental study of the Ostwald ripening of vapor bubbles in magmas.
717 Contributions to Mineralogy and Petrology, 161, 331–347.
718 Lesne, P., Scaillet, B., Pichavant, M., Beny, J.-M. (2011) The carbon dioxide solubility in
719 alkali basalts: an experimental study. Contributions to Mineralogy and Petrology,
720 162, 153–168.
721 Liu, X., O'Neill, H.St.C., and Berry, A.J. (2006) The effects of small amounts of H_2O,
722 CO_2 and Na_2O on the partial melting of spinel lherzolite in the system CaO-MgO-
723 Al_2O_3-SiO_2 ± H_2O ± CO_2 ± Na_2O at 1.1 GPa. Journal of Petrology, 47, 409–434.
724 doi:10.1093/petrology/egi081
725 Lowenstern, J.B. (2001) Carbon dioxide in magmas and implications for hydrothermal
726 systems. Mineralium Deposita, 36, 490–502. doi/10.1007/s001260100185
727 Mangan, M.T., Miller, T., Waythomas, C., Trusdell, F., Calvert, A., and Layer, P. (2009)
728 Diverse lavas from closely spaced volcanoes drawing from a common parent:

729 Emmons Lake Volcanic Center, Eastern Aleutian Arc. Earth and Planetary Science
730 Letters, 287, 363–372. doi:10.1016/j.epsl.2009.08.018
731 Mangan, M.T., Cashman, K.V., and Swanson, D.A. (2014) The dynamics of Hawaiian-
732 style eruptions: A century of study. In M.P. Poland, T.J. Takahashi, and C.M.
733 Landowski, Eds., Characteristics of Hawaiian Volcanoes, U.S. Geological Survey
734 Professional Paper 1801, 323–354, http://dx.doi.org/10.3133/pp1801
735 Mastin, L.G. (1997) Evidence for water influx from a caldera lake during the explosive
736 hydromagmatic eruption of 1790, Kilauea Volcano, Hawaii. Journal of Geophysical
737 Research, 102-B9, 20093–20109.
738 Mastin, L.G., Christiansen, R.L., Thornber, C., Lowenstern, J.B., and Beeson, M. (2004)
739 What makes hydromagmatic eruptions violent? Some insights from the Keanakakoi
740 Ash, Kilauea Volcano, Hawaii. Journal of Volcanology and Geothermal Research,
741 137, 15–31.
742 McNutt, S.R., and Beavan, R.J. (1987) Eruptions of Pavlof Volcano and their possible
743 modulation by ocean load and tectonic stresses. Journal of Geophysical Research, 92-
744 B11, 11509–11523.
745 McNutt, S.R., and Jacob, K.H. (1986) Determination of large-scale velocity structure of
746 the crust and upper mantle in the vicinity of Pavlof volcano, Alaska. Journal of
747 Geophysical Research, 91-B5, 5013–5022.
748 Métrich, N., and Wallace, P.J. (2008) Volatile abundances in basaltic magma and their
749 degassing paths tracked by melt inclusions. In K.D. Putirka and F.J. Tepley III, Eds.,
750 Minerals, Inclusions and Volcanic Processes, Reviews in Mineralogy and

751 Geochemistry, 69, p. 363–402, Mineralogical Society of America, Chantilly,
752 Virginia.
753 Moore, G. (2008) Interpreting H_2O and CO_2 contents in melt inclusions: Constraints from
754 solubility experiments and modeling. In K.D. Putirka and F.J. Tepley III, Eds.,
755 Minerals, Inclusions and Volcanic Processes, Reviews in Mineralogy and
756 Geochemistry, 69, p. 333–361, Mineralogical Society of America, Chantilly,
757 Virginia.
758 Ni, H., and Keppler, H. (2013) Carbon in Silicate Melts. In R.M. Hazen, A.P. Jones, and
759 J.A. Baross, Eds., Carbon in Earth, Reviews in Mineralogy and Geochemistry, 75, p.
760 251–287, Mineralogical Society of America, Chantilly, Virginia.
761 Nye, C.J., and Reid, M.R. (1986) Geochemistry of primary and least fractionated lavas
762 from Okmok Volcano, central Aleutians: Implications for arc magmagenesis. Journal
763 of Geophysical Research, 91, 10271–10287.
764 Papale, P., Moretti, R., and Barbato, D. (2006) The compositional dependence of the
765 saturation surface of H_2O + CO_2 fluids in silicate melts. Chemical Geology, 229, 78–
766 95.
767 Polacci, M., Baker, D., Mancini, L., Tromba, G., and Zanini, F. (2006) Three-
768 dimensional investigation of volcanic textures by X-ray microtomography and
769 implication for conduit processes. Geophysical Research Letters, 33, L13312.
770 doi:10.1029/2006GL026241
771 Power, J.A, Stihler, S.D., White, R.A., and Moran, S.C. (2004) Observations of deep
772 long-period (DLP) seismic events beneath Aleutian arc volcanoes: 1989-2002.
773 Journal of Volcanology and Geothermal Research, 138, 243–266.

774 Sable, J.E., Houghton, B.F., Del Carlo, P., and Coltelli, M. (2006) Changing conditions
775 of magma ascent and fragmentation during the Etna 122 BC basaltic Plinian eruption;
776 evidence from clast microtextures. Journal of Volcanology and Geothermal Research,
777 158, 333–354. doi:10:1016/j.jvolgeores.2006.07.006
778 Saxena, S.K., and Fei, Y. (1987) High pressure and high temperature fluid fugacities.
779 Geochimica et Cosmochimica Acta, 51, 783–791.
780 Shishkina, T.A., Botcharnikov, R.E., Holtz, F., Almeev, R.R., and Portnyagin, M.V.
781 (2010) Solubility of H_2O- and CO_2-bearing fluids in tholeiitic basalts at pressures up
782 to 500 MPa. Chemical Geology, 277, 115–125. doi:10.1016/j.chemgeo.2010.07014
783 Sisson, T.W., Ratajeski, K., Hankins, W.B., and Glazner, A.F. (2005) Voluminous
784 granitic magmas from common basaltic sources. Contributions to Mineralogy and
785 Petrology, 148, 635-661. doi:10.1007/s004100050155
786 Sterner, S.M., and Bodnar, R.J. (1991) Synthetic fluid inclusions. X: Experimental
787 determination of P-V-T-X properties in the CO_2-H_2O system to 6 kb and 700°C.
788 American Journal of Science, 291, 1–54.
789 Ussing, N.V., 1912, Geology of the country around Julianehaab, Greenland. Medd. Om
790 Grønland, 38, 426pp.
791 Vennemann, T.W., and O'Neil, J.R. (1993) A simple and inexpensive method of
792 hydrogen isotope and water analyses of minerals and rocks based on zinc reagent.
793 Chemical Geology, 103, 227–234.
794 Vetere, F., Botcharnikov, R.E., Holtz, F., Behrens, H., and De Rosa, R. (2011) Solubility
795 of H_2O and CO_2 in shoshonitic melts at 1250°C and pressures from 50 to 400 MPa:

Implications for Campi Flegrei magmatic systems. Journal of Volcanology and Geothermal research, 202, 251–261. doi:10.1016/j.volgeores.2011.03.002

Wallace, P.J. (2004) Volatiles in subduction zone magmas: concentrations and fluxes based on melt inclusion and volcanic gas data. Journal of Volcanology and Geothermal Research, 140, 217–240.

Waythomas, C.F., Haney, M.M., Wallace, K.L., Cameron, C.E., and Schneider, D.J. (2017) The 2014 eruptions of Pavlof Volcano, Alaska. U.S. Geological Survey Scientific Investigations Report 2017–5129, 27 p. https://pubs.usgs.gov/sir/2017/5129/sir20175129

Zhang, Y., and Ni, H. (2010) Diffusion of H, C, and O components in silicate melts. In Y. Zang, and D.J. Cherniak, Eds., Diffusion in Minerals and Melts, Reviews in Mineralogy and Geochemistry, 72, p. 171–225, Mineralogical Society of America, Chantilly, Virginia.

Zimmer, M.M., Plank, T., Hauri, E.H., Yogodzinski, G.M., Stelling, P., Larsen, J., Singer, B., Jicha, B., Mandeville, C., and Nye, C.J. (2010) The role of water in generating the calc-alkaline trend: New volatile data for Aleutian magmas and a new tholeiitic index. Journal of Petrology, 51, 2411–2444, doi:10.1093/petrology/egq062

FIGURE CAPTIONS

Figure 1. Photomicrographs of decompression glasses. Cross-sections through capsules are on the left with corresponding close-up images shown on the right. The upper pair of images shows uniform bubble size and distribution (run #1919); bubbles in the lower pair of images (#1962) are heterogeneous in size and distribution due to coalescence and segregation over longer dwell times at P_{final} (30 s versus 3750 s for #1919 and #1962, respectively). Left and right scale bars apply to top and bottom images.

Figure 2. FTIR spectrum of quenched glass from run # 1910. Sample thickness was 28 μm. Absorbance is equal to the logarithm of the measured IR signal through the reference spectrum (air) divided by the sample spectrum (air plus sample).

Figure 3. Concentrations of dissolved CO_2 (ppmw) versus dissolved H_2O (wt.%) for solubility experiments conducted at 1125 °C and total pressures of 310–1200 MPa in basaltic andesite melt. Error bars are 2-sigma uncertainties. Results are subdivided by total run pressure.

Figure 4. (A) Experimental total pressure (P_{total}) plotted against dissolved CO_2 concentrations (ppmw) in experimental glasses measured by ion microprobe, with 2-sigma concentration uncertainties (some error bars are smaller than data symbol). Glasses are subdivided by dissolved H_2O concentrations. (B) Calculated H_2O pressure (P_{H_2O}) in the fluid plotted against dissolved H_2O concentration (wt.%) in glasses measured by ion microprobe, with 2-sigma concentration uncertainties. Glasses are

837 subdivided by run pressure. (C) Calculated CO_2 pressure (P_{CO_2}) in the fluid plotted
838 against dissolved CO_2 concentration (ppmw) in glasses measured by ion microprobe,
839 with 2-sigma concentration uncertainties. Glasses are subdivided by dissolved H_2O
840 concentrations. Plotted H_2O and CO_2 fluid-pressure values in B and C are mid-points of
841 derivations from Ghiorso and Gualda (2015) and Papale et al. (2006) H_2O solubility
842 models, as described in text, with uncertainty bars showing solution ranges; dotted lines
843 in B and C are unweighted power-law regressions yielding the indicated equations,
844 chiefly for reference.
845
846 Figure 5. Experimental total pressure (P_{total}) plotted against CO_2 fugacity (f_{CO_2})
847 estimated as per text; symbols are plotted at the mid-points of f_{CO_2} values calculated
848 using Ghiorso and Gualda (2015) and Papale et al. (2006) H_2O solubility models with
849 error bars indicating solution ranges; glasses are subdivided by dissolved H_2O
850 concentrations. Curves show $f_{CO_2} - P_{total}$ relations of the Churakov and Gottschalk
851 (2003a, b) fluid equation of state applied to binary H_2O-CO_2 fluids at 1125 °C with the
852 indicated mol fractions of CO_2.
853
854 Figure 6. Calculated CO_2 fugacity versus measured dissolved CO_2 concentrations for
855 hydrous solubility experiments conducted at 1125 °C and total pressures of 310 to 1200
856 MPa (colored symbols, differentiated by dissolved H_2O as in Fig. 4). As per text,
857 Ghiorso and Gualda (2015) H_2O solubility model was used to estimate of $X_{H_2O}^{fluid}$ and
858 $P_{H_2O}^{fluid}$, and then by difference, $X_{CO_2}^{fluid}$ and $P_{CO_2}^{fluid}$ were calculated; subsequent f_{CO_2}

values were obtained using Churakov and Gottschalk (2003a, b). Vertical lines are 2-sigma CO_2 concentration uncertainties for each data point (some error bars are smaller than data symbol). Dashed black line shows regression to all results:

$$\log_{10} CO_2\ (ppmw) = 1.1746(\pm 0.1146) + 0.6976(\pm 0.0314) \times \log_{10} f_{CO_2}\ (MPa)$$

and ignores individual measurement uncertainties. Dashed gray lines propagate 1-standard error of the regression.

Figure 7. Comparison of Pavlof experiments (colored symbols, differentiated by dissolved H_2O as in Fig. 4) with solubility models of Papale et al. (2006) (long-dashed curves, P), Iacono-Marziano, et al. (2012) (short-dashed curves, IM), and Ghiorso and Gualda (2015) (solid curves, GG). Model CO_2 solubilities were calculated for the Pavlof basaltic andesite composition as a melt with 2, 4, and 6 wt.% dissolved H_2O at 1125 °C and 400, 600, 800, 1000 MPa (and 1200 MPa for the Ghiorso and Gualda model), the f_{CO_2} was determined from the H_2O and CO_2 mol fractions in the fluid at the model pressure as per Churakov and Gottschalk (2003a, b), and fit to curves subdivided by H_2O concentrations denoted by 2 %, 4 %, and 6 % on the curve labels.

Figure 8. Synthetic H_2O-CO_2 concentration isobars (black lines) at indicated fluid saturation pressures (400–1200 MPa) for Pavlof basaltic andesite melt at 1125 °C and f_{O_2} of Ni-NiO, calculated with the Ghiorso and Gualda (2015) solubility model. Solubility models of Papale et al. (2006) and Iacono-Marziano et al. (2012) give similar-

882 shaped results but that differ in detail. Isopleths of constant f_{CO_2} (dashed gray lines in
883 GPa) are calculated from the saturated fluid compositions, temperature, and total
884 pressure, using the mixed-fluid fugacity model of Churakov and Gottschalk (2003a, b)
885 through the web-based application at http://fluid-
886 eos.web.psi.ch/EOS/calculator_simple.html.
887
888 Figure 9. Comparison of CO_2 concentrations in hydrous basaltic melts experimentally
889 equilibrated with a CO_2-rich gas/fluid phase ($X_{CO_2}^{fluid}$ = 0.46–0.93) covering experimental
890 f_{CO_2} between 350–2685 MPa (300–610 MPa total pressure) and 1125–1250 °C. Range
891 of dissolved H_2O for each experimental suite is given in parentheses. Data for Mutnovsky
892 tholeiite is from Shishkina et al. (2010); Etna alkali basalt from Iacono-Marziano et al.
893 (2012); other compositions (with the exception of our Pavlof basaltic andesite) are from
894 Allison et al. (2019). The f_{O_2} conditions for all experiments were near Ni-NiO, with the
895 exception of Iacono-Marziano et al. (2012) in which f_{O_2} is reported only as "> FMQ+1."
896 For internal consistency, all f_{CO_2} values were calculated using the model of Churakov
897 and Gottschalk (2003a, b) using values of temperature, total pressure, and the fluid's mol
898 fraction CO_2 as reported by the authors. Dashed lines are linear fits to the data. To the
899 right of the trendlines, "agpaitic indices" (molar (Na+K+Ca)/Al) are given for each melt
900 composition.
901
902 Figure 10. Comparison of CO_2 concentrations in hydrous basaltic andesite (this study)
903 and icelandite (Jakobsson, 1997) covering experimental f_{CO_2} between 4000–25000 MPa
904 (720–1200 MPa total pressure); CO_2-rich fluid for both suites are in the range $X_{CO_2}^{fluid}$ =

905 0.66–0.93. Ranges of dissolved H_2O in the experimental melts are as shown. For
906 consistency, the published Jakobsson f_{CO_2} values were recast using the model of
907 Churakov and Gottschalk (2003a, b). Dashed line is a curve fit to the subset of the Pavlof
908 data plotted.

TABLE 1. Composition of starting material

Oxide	wt.%
SiO_2	52.6
TiO_2	1.22
Al_2O_3	18.4
FeO_{total}	9.67
MnO	0.20
MgO	4.72
CaO	8.93
Na_2O	3.40
K_2O	0.62
P_2O_5	0.29

Bulk composition in weight percent oxides by XRF for Pavlof lava sample 03S75M1 in Mangan et al., 2009; FeO_{total} is all iron reported as FeO, and the analysis is normalized to 100 wt.% volatile-free.

This is the peer-reviewed, final accepted version for American Mineralogist, published by the Mineralogical Society of America.
The published version is subject to change. Cite as Authors (Year) Title. American Mineralogist, in press.
DOI: https://doi.org/10.2138/am-2021-7531. http://www.minsocam.org/

TABLE 2. Fluid buffers

Fluid buffer	Volatiles added to inner capsule [wt.%]	Anticipated CO_2:H_2O for fluid in equilibrium with melt [molar]	Volatile buffer added to outer capsule [wt.%]
#1	2 % H_2O + 1 % CO_2	80:20:00	87 %$Ag_2{\cdot}2(CO_2)$ + 13 % $C_2H_2O_4$
#2	4 % H_2O + 1 % CO_2	70:30:00	66 % $Ag_2{\cdot}2(CO_2)$ + 34 % $C_2H_2O_4$
#3	6 % H_2O + 1 % CO_2	60:40:00	100 % $C_2H_2O_4{\cdot}2(H_2O)$

One of three fluid buffers were added to the outer capsules. The buffer selected for each run matched the anticipated equilibrated fluid composition as calculated by the solubility model of Papale et al. (2006) for 2, 4, or 6 wt.% H_2O and 1 wt.% CO_2 added to inner capsule.

This is the peer-reviewed, final accepted version for American Mineralogist, published by the Mineralogical Society of America.
The published version is subject to change. Cite as Authors (Year) Title. American Mineralogist, in press.
DOI: https://doi.org/10.2138/am-2021-7531. http://www.minsocam.org/

TABLE 3. Major element composition (wt.%) of experimental glasses

Run #	1892	1890	1894	Average glass
Run pressure	330 MPa	533 MPa	884 MPa	composition
SiO_2	52.9 ±0.2	53.0 ±0.20	53.1 ±0.3	53.0 ±0.1
TiO_2	1.22 ±0.10	1.15 ±0.07	1.14 ±0.11	1.17 ±0.05
Al_2O_3	18.8 ±0.1	19.0 ±0.1	19.0 ±0.2	18.9 ±0.1
FeO_{total}	9.21 ±0.14	8.82 ±0.17	8.84 ±0.19	8.96 ±0.22
MnO	0.23 ±0.05	0.30 ±0.05	0.31 ±0.07	0.28 ±0.04
MgO	4.49 ±0.05	4.53 ±0.07	4.47 ±0.06	4.50 ±0.03
CaO	8.99 ±0.10	8.98 ±0.11	8.86 ±0.09	8.94 ±0.07
Na_2O	3.48 ±0.11	3.55 ±0.13	3.62 ±0.08	3.54 ±0.07
K_2O	0.61 ±0.03	0.60 ±0.03	0.60 ±0.03	0.60 ±0.01
SO_3	0.01 ±0.01	0.02 ±0.01	0.01 ±0.01	0.01 ±0.01
Cl	0.04 ±0.01	0.03 ±0.01	0.04 ±0.01	0.04 ±0.0
Original sum	96.0 ±0.30	95.1 ±0.40	95.7 ±0.4	95.6 ±0.40

Glass analyses by electron microprobe. Standard deviations of multiple analysis points are reported as ± wt.%. Compositions were normalized to 100 wt.%; original summations are reported in the final row. Equilibration pressure for each run is given in the second row. All three runs equilibrated with 2 wt.% H_2O and 1 wt.% CO_2 added to the inner capsule; outer capsules contained buffer composition #1.

This is the peer-reviewed, final accepted version for American Mineralogist, published by the Mineralogical Society of America.
The published version is subject to change. Cite as Authors (Year) Title. American Mineralogist, in press.
DOI: https://doi.org/10.2138/am-2021-7531. http://www.minsocam.org/

TABLE 4. Decompression results

Run #	Dwell time [s]	Porosity [vol.%]	Bubble diameter [mm]	Bubble number density [bubbles/mm^3]	Glass texture
1916	< 1	< 1	≤ 0.001	≤ 1x10^0	Sparse, ghostly bubble embryos
1919	30	5.0 ±0.5	0.01 ±0.001	1.5x10^4 ± 6x10^3	Uniform bubble distribution
1958	150	4.5 ±0.6	0.02 ±0.003	1.3x10^3 ± 3x10^1	Non-uniform distribution; lower bubble-poor zone
1962	3750	5.1 ±0.3	0.009 ±0.002	2.3x10^2 ±1x10^2	Non-uniform distribution; upper foam layer

After equilibration at 1040 MPa, runs were rapidly decompressed to 310 MPa and then held for various dwell times prior to quenching. The ± values represent standard deviation of multiple measurements of glass porosity, bubble diameter, and bubble number density; values for non-uniform distributions represent bubble-rich areas in upper part of capsule.

This is the peer-reviewed, final accepted version for American Mineralogist, published by the Mineralogical Society of America.
The published version is subject to change. Cite as Authors (Year) Title. American Mineralogist, in press.
DOI: https://doi.org/10.2138/am-2021-7531. http://www.minsocam.org/

TABLE 5. Experimental starting conditions and results

Run #	Pressure [MPa]	+H_2O[a] [wt.%]	+CO_2[a] [wt.%]	Fluid buffer	wt.% H_2O dissolved[b]	ppm CO_2 dissolved[b]	wt.% H_2O dissolved[c]	ppm CO_2 dissolved[c]	wt.% H_2O dissolved[d]	ppm CO_2 dissolved[d]	$X_{CO_2}^{fluid}$[e]	$X_{CO_2}^{fluid}$[f]	$f_{CO_2}[MPa]$[e]	$f_{CO_2}[MPa]$[f]
Blank Experiments (1250 °C)														
1903	885	0	0	none	–	–	–	–	1.13 ±0.33	1122 ±434	–	–	–	–
1913	885	0	0	none	–	–	–	–	0.78 ±0.50	1099 ±149	–	–	–	–
Solubility Experiments (1125 °C)														
1901	310	2	1	1	2.73 ±0.05	1275 ±27	–	–	2.94 ±0.04	2119 ±180	0.68	0.74	510	550
1910	310	4	1	2	3.83 ±0.06	1168 ±62	–	–	3.74 ±0.35	2027 ±306	0.48	0.59	415	445
2112	400	2	1	1	2.29 ±0.13	1136 ±340	–	–	–	–	0.80	0.83	975	1015
2114	400	4	1	2	3.35 ±0.06	1166 ±363	–	–	–	–	0.63	0.72	820	935
2147	385	6	1	3	4.40 ±0.16	1453 ±360	–	–	–	–	0.46	0.57	551	665
2235	520	2	1	1	2.91 ±0.04	2286 ±392	–	–	–	–	0.74	0.81	1695	1835
2068	520	4	1	2	–	–	3.76 ±0.08	2600 ±130	–	–	0.63	0.73	1480	1680
2091	600	2	1	1	2.45 ±0.09	3620 ±251	–	–	–	–	0.82	0.87	2685	2825
2092	600	4	1	2	3.73 ±0.09	3417 ±284	–	–	–	–	0.67	0.76	2230	2505
1908	720	4	1	2	3.75 ±0.03	6840 ±106	–	–	5.7 ±0.43	6615 ±405	0.72	0.79	3705	4025
2110	720	2	1	1	2.36 ±0.10	4825 ±366	–	–	–	–	0.85	0.89	4650	4860
2228	720	4	1	2	4.41 ±0.13	3585 ±320	–	–	–	–	0.62	0.74	3280	3785
2151	815	6	1	3	5.16 ±0.12	6098 ±310	–	–	–	–	0.57	0.70	4135	4960
2066	815	2	1	1	–	–	2.55 ±0.05	7400 ±370	–	–	0.84	0.89	6255	6575
2090	815	4	1	2	3.90 ±0.10	6105 ±241	–	–	–	–	0.71	0.80	5345	5965
2233	815	6	1	3	5.47 ±0.18	5006 ±803	–	–	–	–	0.54	0.69	4235	5180
2070	880	4	1	2	–	–	4.11 ±0.08	7500 ±375	–	–	0.70	0.80	6735	7575
2115	870	2	1	1	2.34 ±0.11	7852 ±622	–	–	–	–	0.87	0.90	7815	8145
2065	1015	2	1	1	–	–	2.90 ±0.06	12500 ±625	–	–	0.83	0.89	12750	13545
1898	1040	2	1	1	2.83 ±0.11	10986 ±69	–	–	3.04 ±0.05	8645 ±800	0.84	0.89	13720	14540
2062	1030	2	1	1	2.92 ±0.04	11581 ±446	–	–	–	–	0.83	0.89	13370	14215
2229	1035	4	1	2	4.51 ±0.07	12571 ±395	–	–	–	–	0.69	0.80	11300	12900
2243	1030	6	1	3	5.39 ±0.19	10192 ±351	–	–	–	–	0.61	0.75	10135	12140
2088	1200	2	1	1	2.44 ±0.13	13800 ±642	–	–	–	–	0.88	0.93	24550	25645
2089	1200	4	1	2	3.82 ±0.06	12916 ±551	–	–	–	–	0.77	0.86	21825	24030
2131	1200	6	1	3	5.30 ±0.21	13316 ±963	–	–	–	–	0.65	0.79	18685	22080
Decompression Experiments (1125 °C, 1040 to 310 MPa)[g]														
1916	g	2	1	1	–	–	–	–	2.8 ±0.10	4003 ±88	–	–	–	–
1919	g	2	1	1	1.37 ±0.11	4893 ±647	–	–	–	–	–	–	–	–
1958	g	2	1	1	2.67 ±0.10	4452 ±430	–	–	–	–	–	–	–	–
1962	g	2	1	1	2.03 ±0.07	1922 ±203	–	–	–	–	–	–	–	–

Fluid buffer types in Table 2. Blank experiments were without added volatiles or fluid buffers. Uncertainties are given as ± values. FTIR concentration uncertainties reflect variation within a single glass wafer (6 analysis areas per wafer); IMS uncertainties are point-to-point glass variability plus uncertainty in IMS calibration curves; manometry concentrations

are reported with relative error from calibration of the technique (5 % of H_2O and 2 % of CO_2 determined). Mol fractions of CO_2 in fluid ($X_{CO_2}^{fluid}$) and fugacity of CO_2 (f_{CO_2}) are calculated for two different H_2O solubility models as per text. Dashes indicate values not determined.

Footnotes:

a. Amounts of H_2O [wt.%] and CO_2 [ppm] added to Pavlof basaltic andesite.
b. Measured in glass by IMS
c. Measured in glass by manometry
d. Measured in glass by FTIR.
e. Mol fraction CO_2 in fluid and CO_2 fugacity calculated with Ghiorso and Gualda (2015) H_2O solubility model.
f. Mol fraction CO_2 in fluid and CO_2 fugacity calculated with Papale et al. (2006) H_2O solubility model.
g. Equilibration at 1040 MPa followed by decompression to and quenching at 310 MPa.

This is the peer-reviewed, final accepted version for American Mineralogist, published by the Mineralogical Society of America.
The published version is subject to change. Cite as Authors (Year) Title. American Mineralogist, in press.
DOI: https://doi.org/10.2138/am-2021-7531. http://www.minsocam.org/

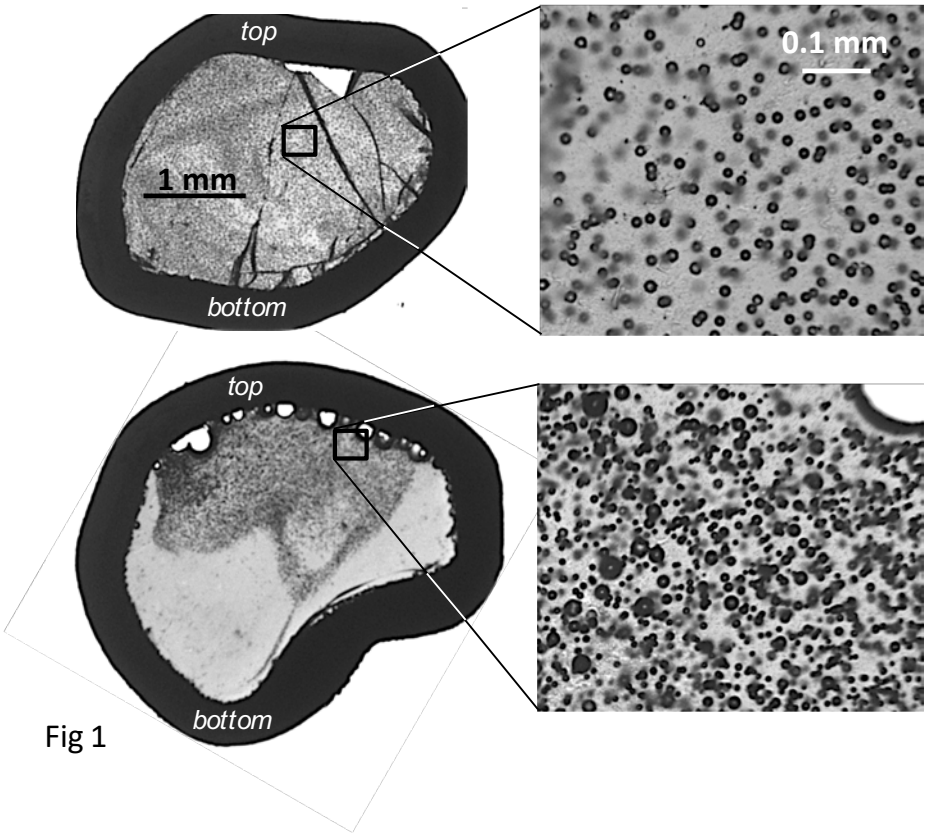

Figure 1. Photomicrographs of decompression glasses. Cross-sections through capsules are on the left with corresponding close-up images shown on the right. The upper pair of images shows uniform bubble size and distribution (run #1919); bubbles in the lower pair of images (#1962) are heterogeneous in size and distribution due to coalescence and segregation over longer dwell times at P_{final} (30 s versus 3750 s for #1919 and #1962, respectively). Left and right scale bars apply to top and bottom images.

This is the peer-reviewed, final accepted version for American Mineralogist, published by the Mineralogical Society of America.
The published version is subject to change. Cite as Authors (Year) Title. American Mineralogist, in press.
DOI: https://doi.org/10.2138/am-2021-7531. http://www.minsocam.org/

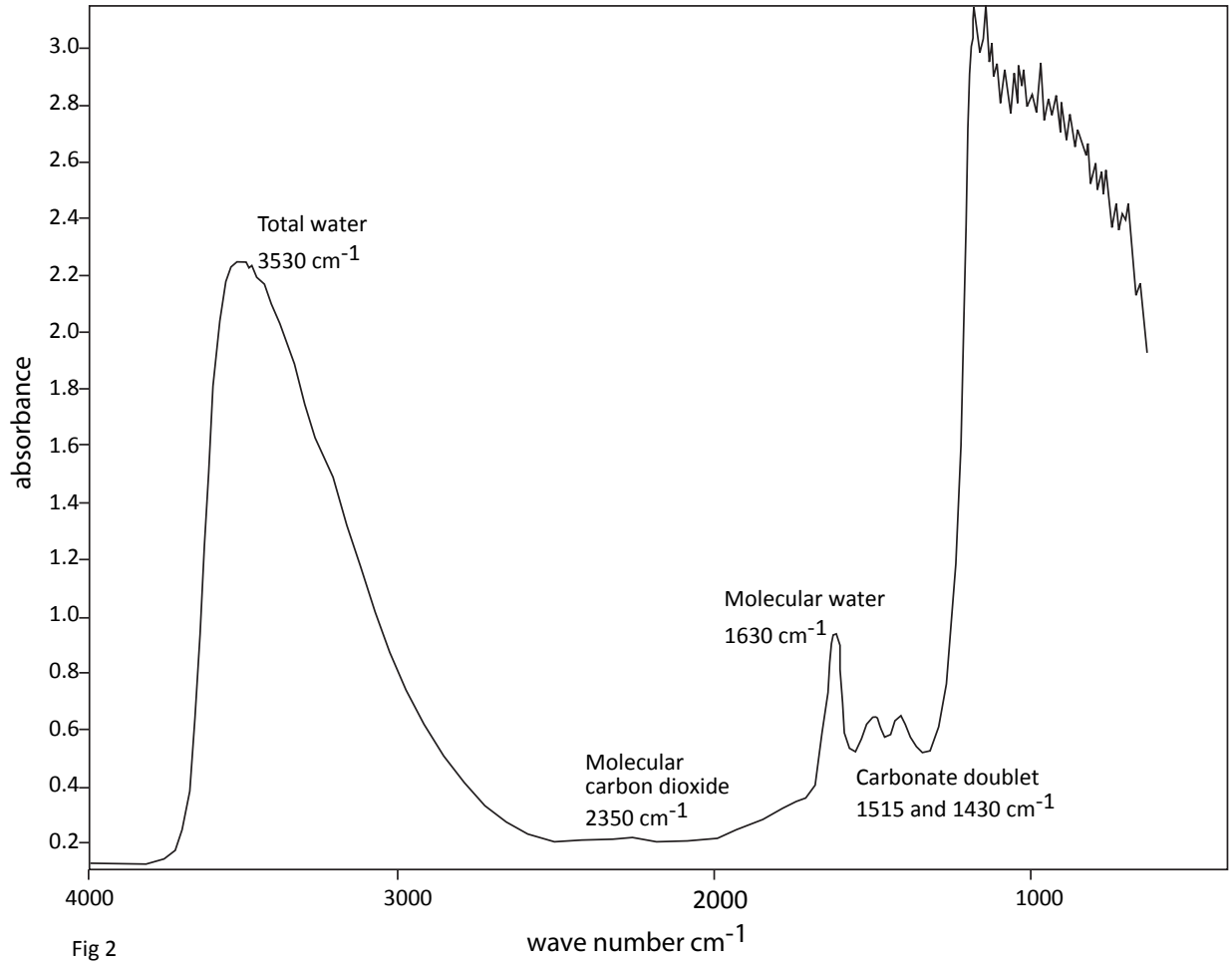

Figure 2. FTIR spectrum of quenched glass from run # 1910. Sample thickness was 28 μm. Absorbance is equal to the logarithm of the measured IR signal through the reference spectrum (air) divided by the sample spectrum (air plus sample).

This is the peer-reviewed, final accepted version for American Mineralogist, published by the Mineralogical Society of America.
The published version is subject to change. Cite as Authors (Year) Title. American Mineralogist, in press.
DOI: https://doi.org/10.2138/am-2021-7531. http://www.minsocam.org/

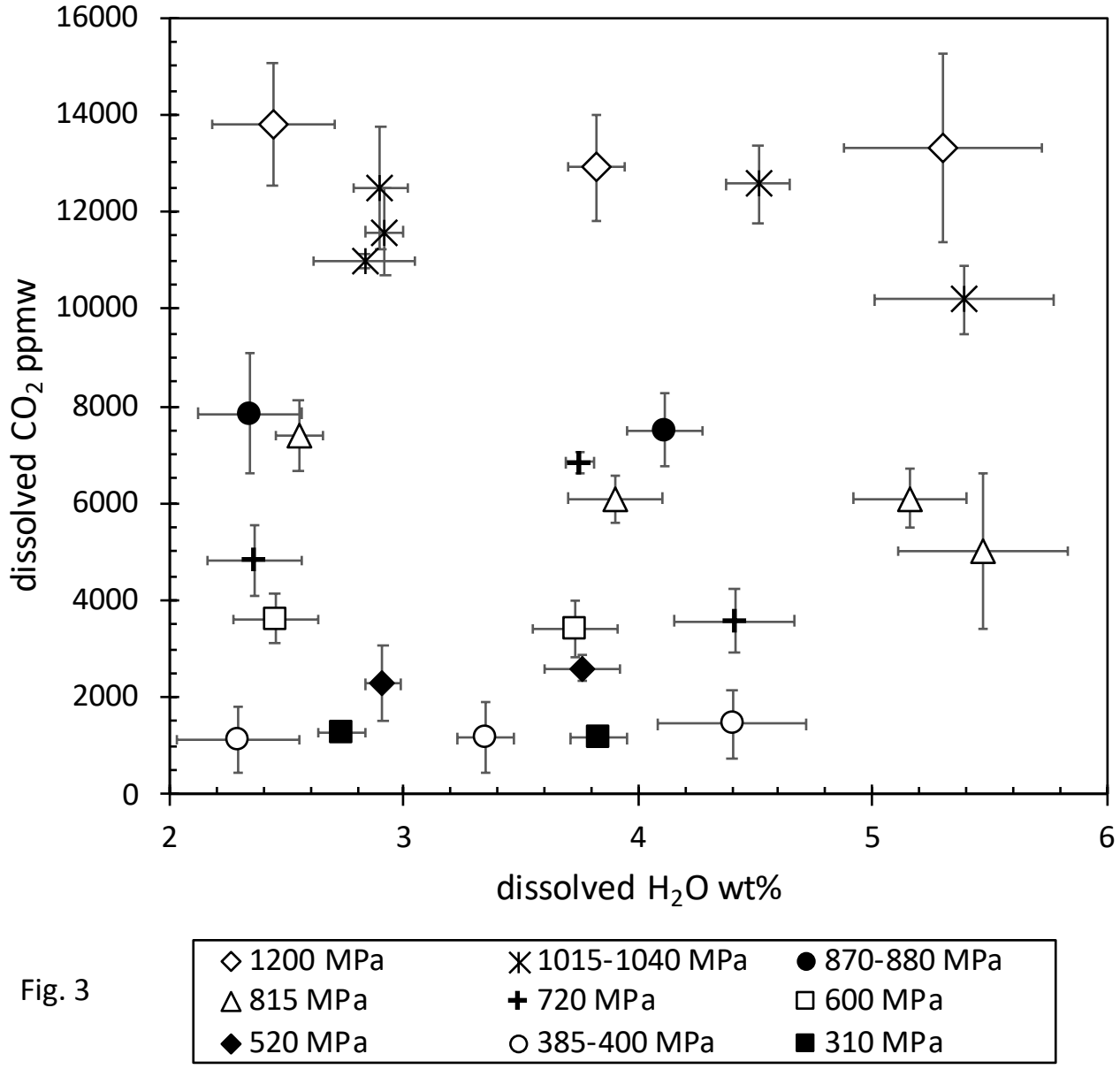

Fig. 3

Figure 3. Concentrations of dissolved CO_2 (ppmw) versus dissolved H_2O (wt.%) for solubility experiments conducted at 1125 °C and total pressures of 310–1200 MPa in basaltic andesite melt. Error bars are 2-sigma uncertainties. Results are subdivided by total run pressure.

This is the peer-reviewed, final accepted version for American Mineralogist, published by the Mineralogical Society of America.
The published version is subject to change. Cite as Authors (Year) Title. American Mineralogist, in press.
DOI: https://doi.org/10.2138/am-2021-7531. http://www.minsocam.org/

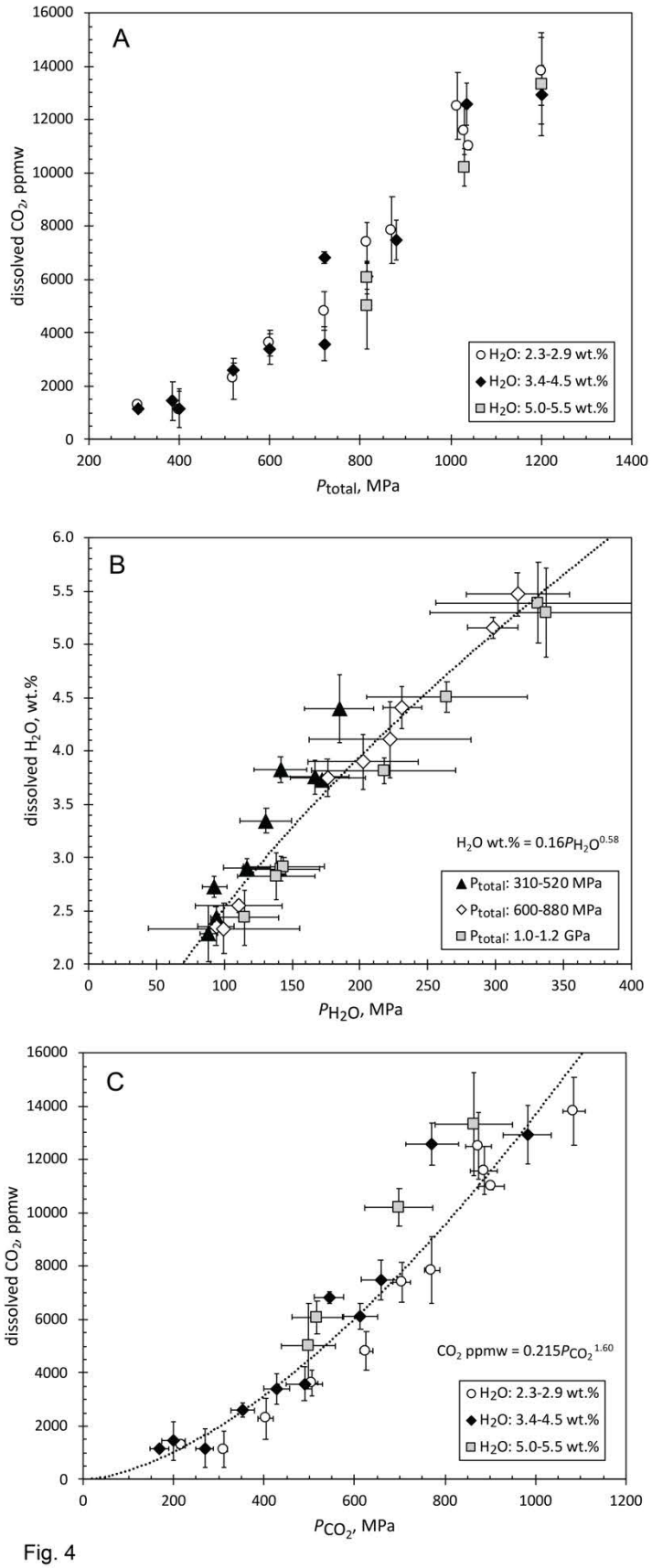

Fig. 4

Figure 4. (A) Experimental total pressure (P_{total}) plotted against dissolved CO_2 concentrations (ppmw) in experimental glasses measured by ion microprobe, with 2-sigma concentration uncertainties (some error bars are smaller than data symbols). Glasses are subdivided by dissolved H_2O concentrations. (B) Calculated H_2O pressure (P_{H_2O}) in the fluid plotted against dissolved H_2O concentration (wt.%) in glasses measured by ion microprobe, with 2-sigma concentration uncertainties. Glasses are subdivided by run pressure. (C) Calculated CO_2 pressure (P_{CO_2}) in the fluid plotted against dissolved CO_2 concentration (ppmw) in glasses measured by ion microprobe, with 2-sigma concentration uncertainties. Glasses are subdivided by dissolved H_2O concentrations. Plotted H_2O and CO_2 fluid-pressure values in B and C are mid-points of derivations from Ghiorso and Gualda (2015) and Papale et al. (2006) H_2O solubility models, as described in text, with uncertainty bars showing solution ranges; dotted lines in B and C are unweighted power-law regressions yielding the indicated equations, chiefly for reference.

This is the peer-reviewed, final accepted version for American Mineralogist, published by the Mineralogical Society of America.
The published version is subject to change. Cite as Authors (Year) Title. American Mineralogist, in press.
DOI: https://doi.org/10.2138/am-2021-7531. http://www.minsocam.org/

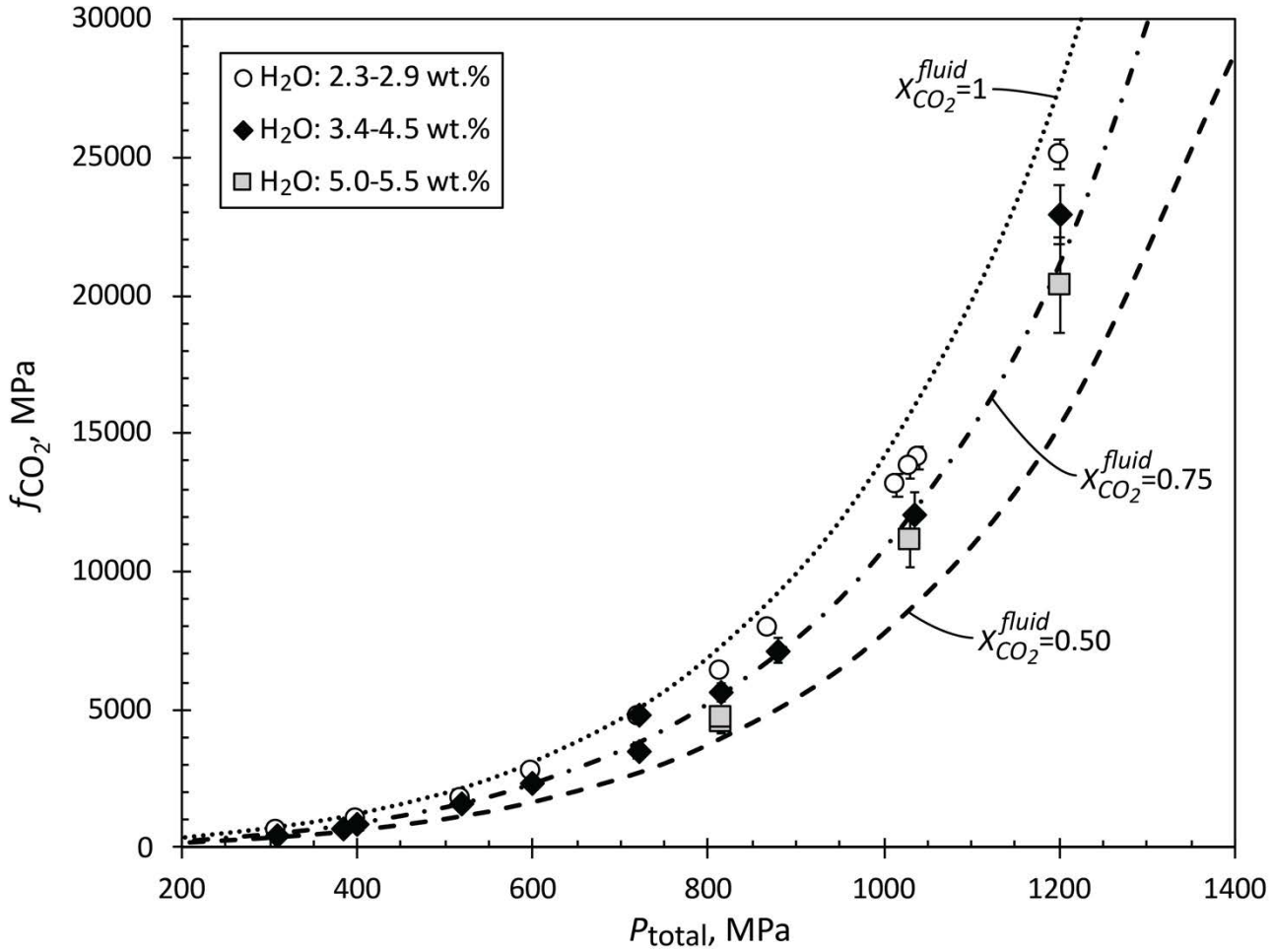

Fig. 5

Figure 5. Experimental total pressure (P_{total}) plotted against CO_2 fugacity (f_{CO_2}) estimated as per text; symbols are plotted at the mid-points of f_{CO_2} values calculated using Ghiorso and Gualda (2015) and Papale et al. (2006) H_2O solubility models with error bars indicating solution ranges; glasses are subdivided by dissolved H_2O concentrations. Curves show $f_{CO_2} - P_{total}$ relations of the Churakov and Gottschalk (2003a, b) fluid equation of state applied to binary H_2O-CO_2 fluids at 1125 °C with the indicated mol fractions of CO_2.

This is the peer-reviewed, final accepted version for American Mineralogist, published by the Mineralogical Society of America.
The published version is subject to change. Cite as Authors (Year) Title. American Mineralogist, in press.
DOI: https://doi.org/10.2138/am-2021-7531. http://www.minsocam.org/

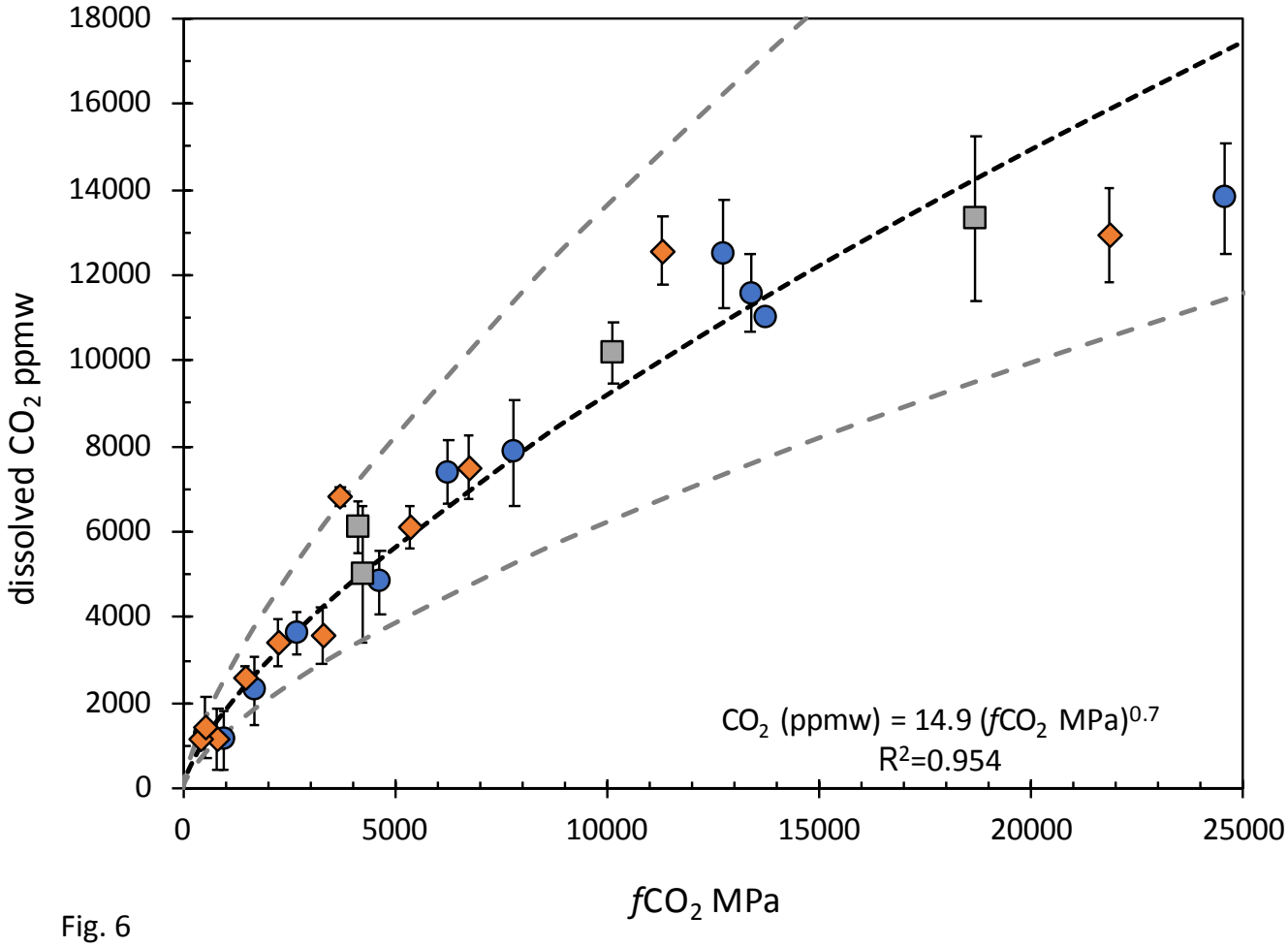

Fig. 6

Figure 6. Calculated CO_2 fugacity versus measured dissolved CO_2 concentrations for hydrous solubility experiments conducted at 1125 °C and total pressures of 310 to 1200 MPa (colored symbols, differentiated by dissolved H_2O as in Fig. 4). As per text, the Ghiorso and Gualda (2015) H_2O solubility model was used to estimate of $X_{H_2O}^{fluid}$ and $P_{H_2O}^{fluid}$, and then by difference, $X_{CO_2}^{fluid}$ and $P_{CO_2}^{fluid}$ were calculated; f_{CO_2} values were then obtained using Churakov and Gottschalk (2003a, b). Vertical lines are 2-sigma CO_2 concentration uncertainties for each data point (some error bars are smaller than data symbol). Dashed black line shows regression to all results:

$$\log_{10} CO_2\ (ppmw) = 1.1746(\pm 0.1146) + 0.6976(\pm 0.0314) \times \log_{10} f_{CO_2}\ (MPa)$$

and ignores individual measurement uncertainties. Dashed gray lines propagate 1-standard error of the regression.

This is the peer-reviewed, final accepted version for American Mineralogist, published by the Mineralogical Society of America.
The published version is subject to change. Cite as Authors (Year) Title. American Mineralogist, in press.
DOI: https://doi.org/10.2138/am-2021-7531. http://www.minsocam.org/

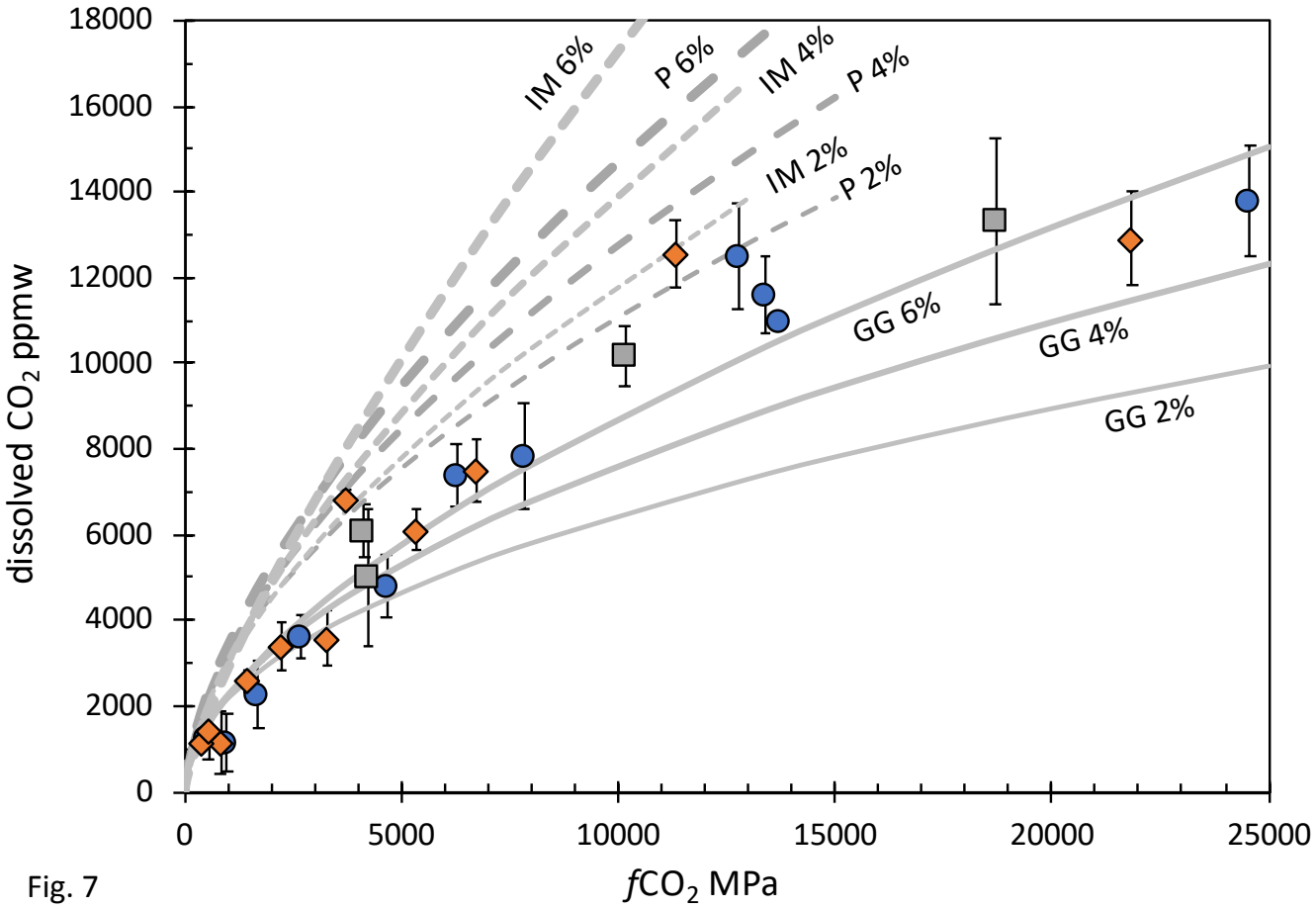

Fig. 7

Figure 7. Comparison of Pavlof experiments (colored symbols, differentiated by dissolved H_2O as in Fig. 4) with solubility models of Papale et al. (2006) (long-dashed curves, P), Iacono-Marziano, et al. (2012) (short-dashed curves, IM), and Ghiorso and Gualda (2015) (solid curves, GG). Model CO_2 solubilities were calculated for the Pavlof basaltic andesite composition as a melt with 2, 4, and 6 wt.% dissolved H_2O at 1125 °C and 400, 600, 800, 1000 MPa (and 1200 MPa for the Ghiorso and Gualda model), the f_{CO_2} was determined from the H_2O and CO_2 mol fractions in the fluid at the model pressure as per Churakov and Gottschalk (2003a, b), and fit to curves subdivided by H_2O concentrations denoted by 2 %, 4 %, and 6 % on the curve labels.

This is the peer-reviewed, final accepted version for American Mineralogist, published by the Mineralogical Society of America.
The published version is subject to change. Cite as Authors (Year) Title. American Mineralogist, in press.
DOI: https://doi.org/10.2138/am-2021-7531. http://www.minsocam.org/

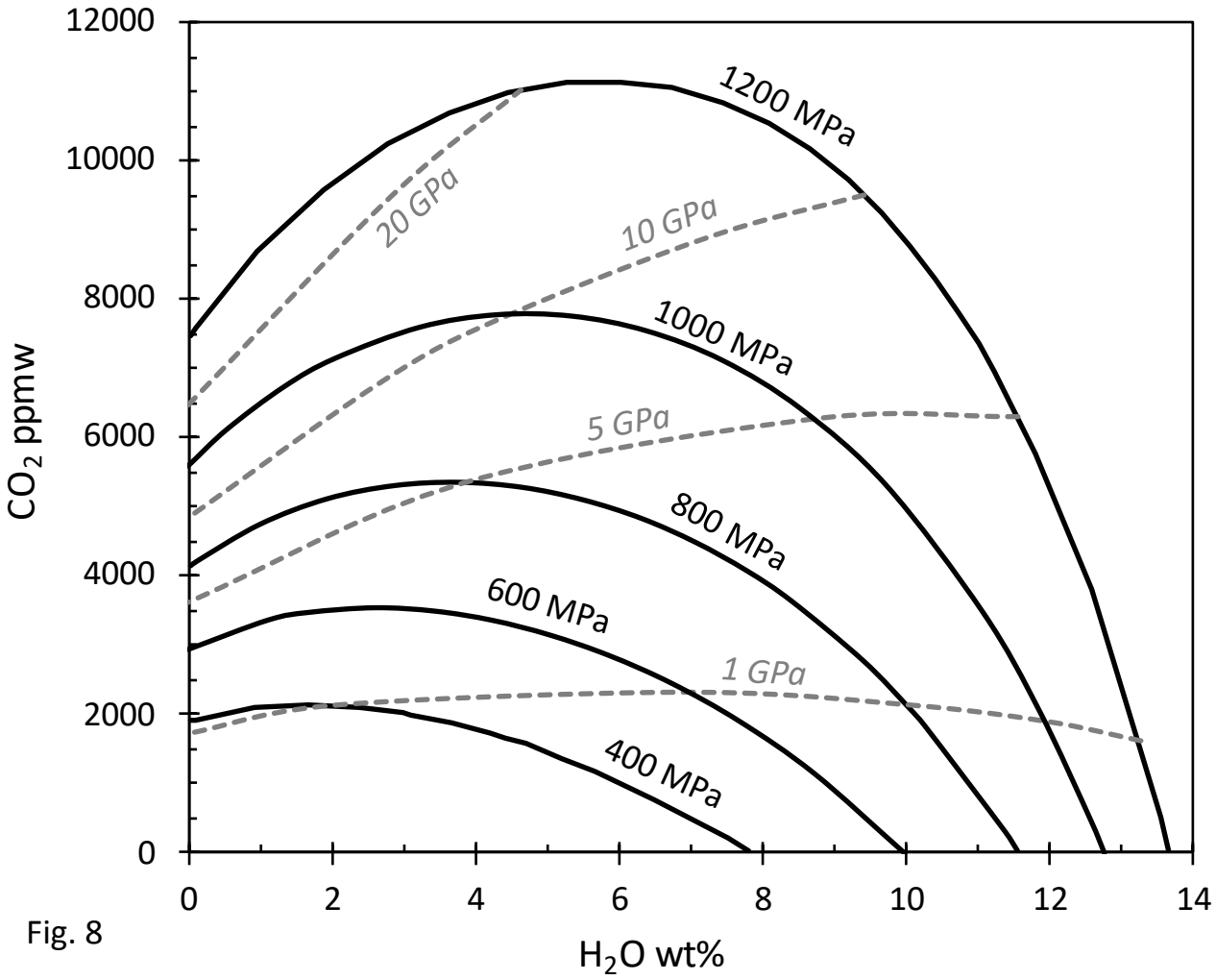

Fig. 8

Figure 8. Synthetic H_2O-CO_2 concentration isobars (black lines) at indicated fluid saturation pressures (400–1200 MPa) for Pavlof basaltic andesite melt at 1125 °C and f_{O_2} of Ni-NiO, calculated with the Ghiorso and Gualda (2015) solubility model. Solubility models of Papale et al. (2006) and Iacono-Marziano et al. (2012) give similar-shaped results but that differ in detail. Isopleths of constant f_{CO_2} (dashed gray lines in GPa) are calculated from the saturated fluid compositions, temperature, and total pressure, using the mixed-fluid fugacity model of Churakov and Gottschalk (2003a, b) through the web-based application at http://fluid-eos.web.psi.ch/EOS/calculator_simple.html.

This is the peer-reviewed, final accepted version for American Mineralogist, published by the Mineralogical Society of America.
The published version is subject to change. Cite as Authors (Year) Title. American Mineralogist, in press.
DOI: https://doi.org/10.2138/am-2021-7531. http://www.minsocam.org/

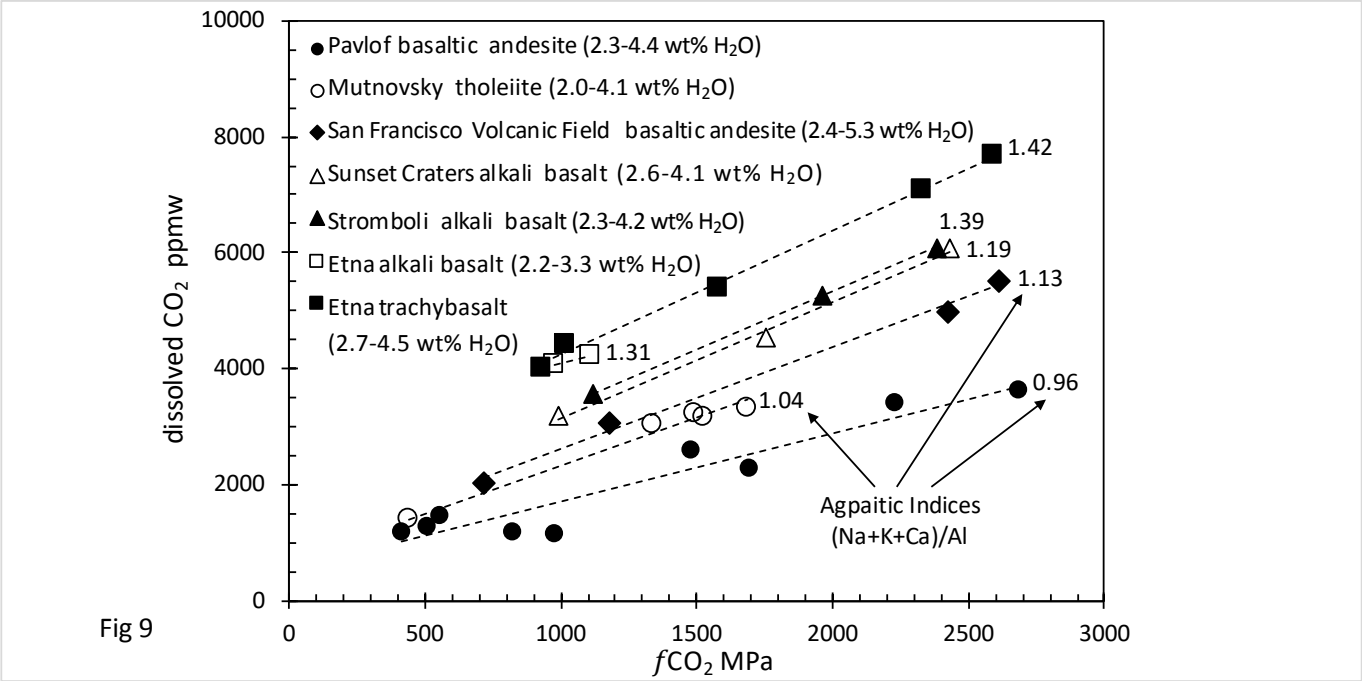

Figure 9. Comparison of CO_2 concentrations in hydrous basaltic melts experimentally equilibrated with a CO_2-rich gas/fluid phase ($X_{CO_2}^{fluid}$ = 0.46–0.93) covering experimental f_{CO_2} between 350–2685 MPa (300–610 MPa total pressure) and 1125–1250 °C. Range of dissolved H_2O for each experimental suite is given in parentheses. Data for Mutnovsky tholeiite is from Shishkina et al. (2010); Etna alkali basalt from Iacono-Marziano et al. (2012); other compositions (with the exception of our Pavlof basaltic andesite) are from Allison et al. (2019). The f_{O_2} conditions for all experiments were near Ni-NiO, with the exception of Iacono-Marziano et al. (2012) in which f_{O_2} is reported only as "> FMQ+1." For internal consistency, all f_{CO_2} values were calculated using the model of Churakov and Gottschalk (2003a, b) using values of temperature, total pressure, and the fluid's mol fraction CO_2 as reported by the authors. Dashed lines are linear fits to the data. To the right of the trendlines, "agpaitic indices" (molar (Na+K+Ca)/Al) are given for each melt composition.

This is the peer-reviewed, final accepted version for American Mineralogist, published by the Mineralogical Society of America.
The published version is subject to change. Cite as Authors (Year) Title. American Mineralogist, in press.
DOI: https://doi.org/10.2138/am-2021-7531. http://www.minsocam.org/

Fig. 10

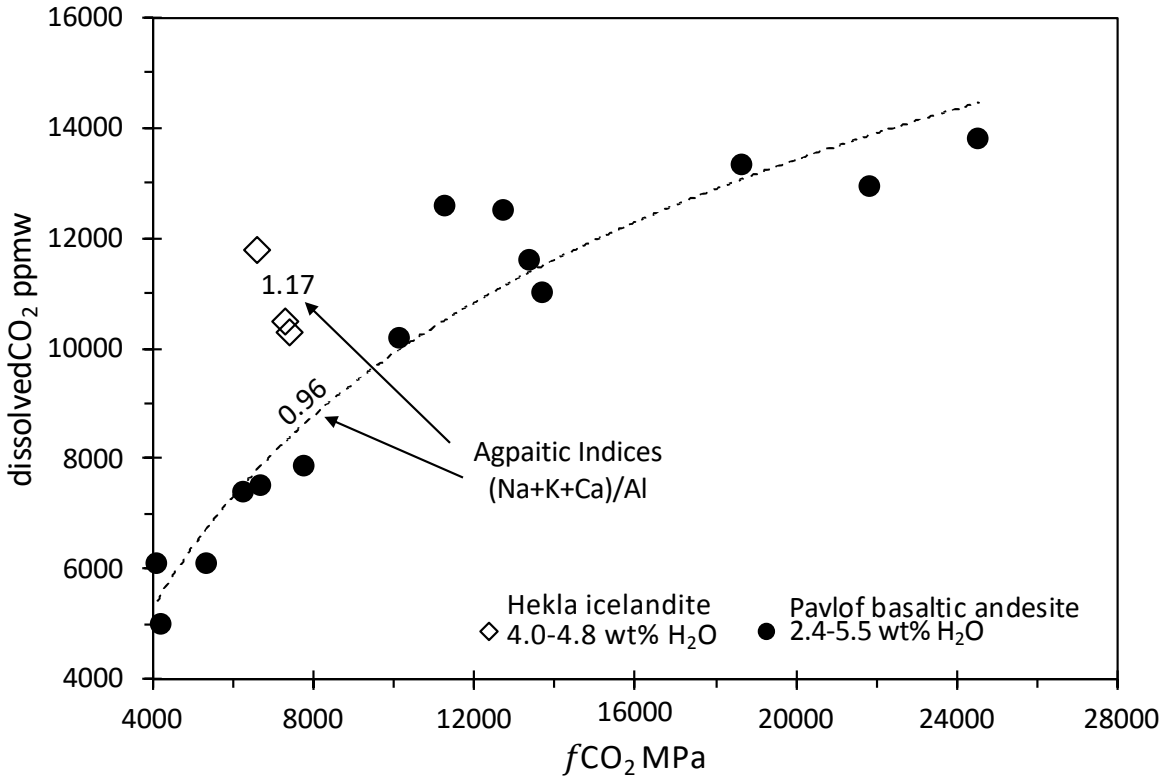

Figure 10. Comparison of CO_2 concentrations in hydrous basaltic andesite (this study) and icelandite (Jakobsson, 1997) covering experimental f_{CO_2} between 4000–25000 MPa (720–1200 MPa total pressure); CO_2-rich fluid for both suites are in the range $X_{CO_2}^{fluid}$ = 0.66–0.93. Ranges of dissolved H_2O in the experimental melts are as shown. For consistency, the published Jakobsson f_{CO_2} values were recast using the model of Churakov and Gottschalk (2003a, b). Dashed line is a curve fit to the subset of the Pavlof data plotted.